COMPUTATIONAL FRAMEWORK FOR MAGNETIC SENSING IN STRUCTURAL HEALTH MONITORING APPLICATIONS VIA MAGNETIC SHAPE MEMORY ALLOYS

A Thesis

by

ALLEN MILLER DAVIS

Submitted to the Office of Graduate and Professional Studies of
Texas A&M University
in partial fulfillment of the requirements for the degree of

MASTER OF SCIENCE

Chair of Committee,	Darren Hartl
Committee Members,	James Boyd
	Douglas Allaire
Head of Department,	Rodney Bowersox

May 2020

Major Subject: Aerospace Engineering

ABSTRACT

In the field of structural health monitoring (SHM), innovative methods of non-destructive evaluation (NDE) are currently being investigated for the purpose of enabling safer, longer lasting structures. While current SHM is dominated by acoustic emission and vibration-based methods, it would be desirable to combine NDE techniques with existing structural reinforcement techniques and allow these two functionalities to combine toward enhancing structural service life. Magnetic shape memory alloys (MSMAs) have differing magnetic properties at different phases related to their stress/strain state. Stress-induced phase transformations in embedded metallic wires, rods, or cables as caused by failure in a surrounding concrete matrix can be correlated to changes in MSMA magnetic properties. A computational model is developed using ABAQUS and COMSOL Multiphysics to evaluate the development of stress-induced martensite (SIM) due to internal damage in a load-bearing concrete-MSMA block composite, which is then shown to lead to a quantitative change in an externally applied magnetic field. This external change in the applied magnetic field, caused by internal damage and the initiation of a local region of SIM, is then used to locate internal damage via measurements of the magnetic flux density on the external surface of the structure. The computational results quantitatively demonstrate a method to locate SIM regions in embedded MSMAs, thus identifying internal structural damage.

DEDICATION

To my mother and father
for fostering in me a sense
of curiosity and excitement
about the world.

CONTRIBUTORS AND FUNDING SOURCES

Contributors

This work was supported by a thesis committee consisting of Professor Darren Hartl and James Boyd of the Department of Aerospace Engineering and Professor Douglas Allaire of the Department of Mechanical Engineering.

As will be noted in this thesis, some material test data was provided by Ibrahim Karaman and his students. Specifically, the material properties of FeMnAlNi used in Chapters 3 and 4 came from work performed by Hande Ozcan, while the material properties of NiCoMnSn particles used in Chapter 5 came from work performed by Nicholas Barta.

Funding Sources

Graduate study was supported by the National Science Foundation (NSF) and the Transportation Consortium of South-Central States (Tran-SET).

NOMENCLATURE

ASTM	American Society for Testing and Materials
AU	Acoustic-ultrasonic
DOE	Design of Experiment
EMA	Effective Medium Approximations
FEA	Finite Element Analysis
FMAN	FeMnAlNi
GMR	Giant Magneto-Resistive
LEFM	Linear Elastic Fracture Mechanics
LLL	Landau-Lifshitz-Looyenga
MGA	Maxwell Garnett Approximation
MSMA	Magnetic Shape Memory Alloy
NDE	Non-Destructive Evaluation
SHM	Structural Health Monitoring
SIM	Stress-Induced Martensite
SMA	Shape Memory Alloy
TMR	Tunnel Magneto-Resistance
XFEM	Extended Finite Element Method

TABLE OF CONTENTS

Page

LIST OF FIGURES

FIGURE Page

LIST OF TABLES

TABLE Page

1. INTRODUCTION

1.1 Structural Health Monitoring

1.1.1 Traditional Structural Health Monitoring

In structures subjected to excessive static or cyclic loading, cracks may develop and propagate leading to eventual structural failure, particularly in materials weak in tension such as concrete [2]. The monitoring of tensile cracks in structures subject to these loading conditions and material limitations is desirable for the monitoring of structures through their lifetime. In recent years, structural health monitoring (SHM), the continuous monitoring of structures in service to detect damage and deterioration before failure, has inspired renewed interest in novel non-destructive evaluation (NDE) techniques with the purpose of extending the service life of structures [3, 4].

Traditionally, external cracks in structures are discovered via physical inspections, often with standardized rating systems and photographic documentation [5, 6]. However, these do not necessarily reveal the presence of internal cracks or the true remaining structural resilience of a structure, which necessitates affordable monitoring systems attached to or embedded within structures throughout their service life [5, 7]. Acoustic sensing methods provide an NDE solution by detecting internal cracks and determining current material fracture properties given a change in the properties of sound waves as they pass through a structure [8, 9, 10]; this allows for external acoustic monitoring of internal cracks. Piezoelectrics have also been implanted in various structural components (e.g., lamina structures [11]) as shown in Fig. 1.1 to both produce and monitor acoustic emissions, providing a related form of integrated NDE. Other external health evaluation work includes embedded inductive sensors developed to monitor the corrosion of internal steel rebar [12], but such a technique requires an applied electric current and provides only the average corrosion between two points.

As a relatively new non-destructive evaluation approach with applicability to SHM, magnetic sensing (i.e., evaluating the external magnetic fields around structural components) has received

particular attention during the past few decades [12, 13]. Studies on monitoring steel corrosion have proven magnetic sensing a viable method of nondestructive evaluation of reinforced concrete structures, with the obtained magnetic signals shown to be significantly strong as compared the background noise present in the system [14]. Giant Magneto-Resistive (GMR) sensors, which measure magnetic field strength, are especially attractive for non-destructive evaluation of the damaged state of steel reinforcements in concrete due to low power consumption and a wide sensing range [14].

Most civil infrastructure relies on reinforced concrete, which accommodates for large cyclical loading by loading the concrete matrix in compression in equilibrium against a reinforcement material, such as steel, in tension. Several studies have been performed to characterize the benefits of various reinforcement forms, such as fibers [15, 16], rebar [17], and braided cables [18], all of which are strong in tension. These structural reinforcement techniques have been shown to increase service life and even close cracks [19]; the current work explores how, through the selection and implementation of a particular multi-functional material in this reinforcement role, additional SHM advantages might be provided.

1.2 Non-Destructive Evaluation of Aircraft

In aircraft, a number of NDE techniques have been explored to detect and monitor structural damage and defects. Acoustic-ultrasonics (AU) utilize acoustic waves in high frequency ranges to limit audible background noise [20], but the interpretation of such acoustic emission signals depends heavily on the data acquisition setup [21]. For aerospace structures with thin plates, wave propagation techniques using Lamb waves have been employed over large areas using changes in both the wave velocity and phase [22, 23]. This technique has been utilized in thin laminate plates by measuring the Lamb wave propagation using a laser scanning vibrometer to detect i) damage due to external impacts by measuring out of plane Lamb wave propagation [23] and ii) fatigue cracks by measuring in-plane Lamb wave propagation [24]. External piezoelectric active sensors have also been used to detect notches in aluminum sheets by measuring the change in amplitude

of applied ultrasonic waves [25]. This technique correlates the change in acoustic signal with the extent of damage, but does not determine the local position of the damage. Additionally, in some cases it may be difficult to differentiate signal changes due to damage or defects from those due to thermal changes in the structure [26].

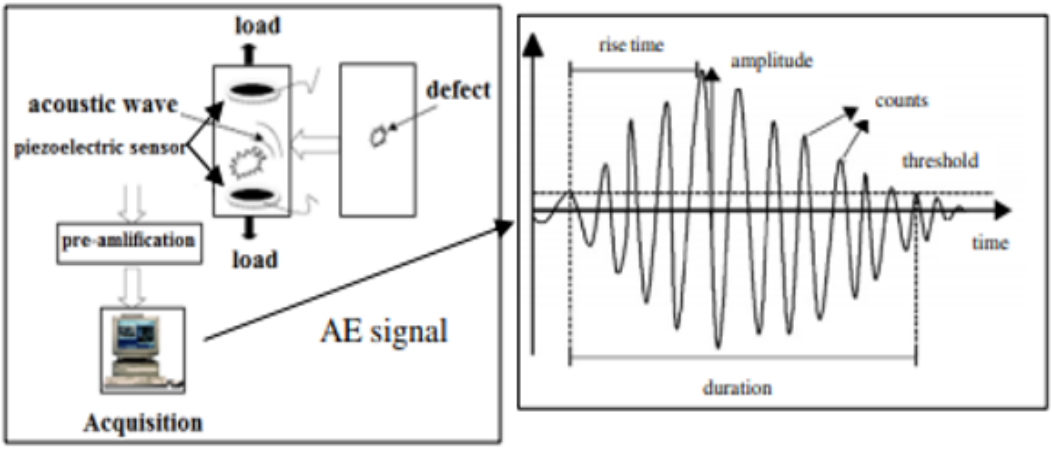

Figure 1.1: Acoustic sensing methods have been developed to determine the existence of internal damage and defects using the combination of a sensor and acoustic wave generator (from [11]).

1.3 Shape Memory Alloys

Shape memory alloys (SMAs) are a class of multi-functional materials that alter their crystallographic state from an austenite to a martensite phase given appropriate stress or temperature stimuli, leading to large and ultimately recoverable strains and the alteration of a number of physical properties [27, 28, 29, 30, 31]. With respect to civil engineering applications, SMA wires have been embedded into concrete structures for structural reinforcement and have been shown to improve the life of structures [19, 32] by taking advantage of their pseudoelastic properties, including large recoverable strains and energetic dampening. SMAs also exhibit reusability [33], which is desirable due to substantially higher production costs than the structural steel used in large-scale construction, and SMA components show high corrosion resistance [34]. Lastly,

SMAs have been shown to reduce fatigue crack growth and delay failure of structures near the end of their life [19, 35]. Given these purely structural advantages, the potential use of embedded SMA components for damage detection to be described is especially attractive when compared to traditional sensing methods.

Magnetic shape memory alloys (MSMAs), a subclass of SMAs that exhibit magneto-mechanical and magneto-thermal coupling, can be influenced by stress fields to alter their magnetic and mechanical properties [36]. For example, MSMAs have been introduced into composite lamina to change the magnetic susceptibility of the lamina under strain-controlled loading [37]. This magneto-mechanical coupling, as exhibited in Fig. 1.2, allows for the alteration of magnetic fields due to a particular change in magnetic permeability in the presence of the internal stress fields [38].

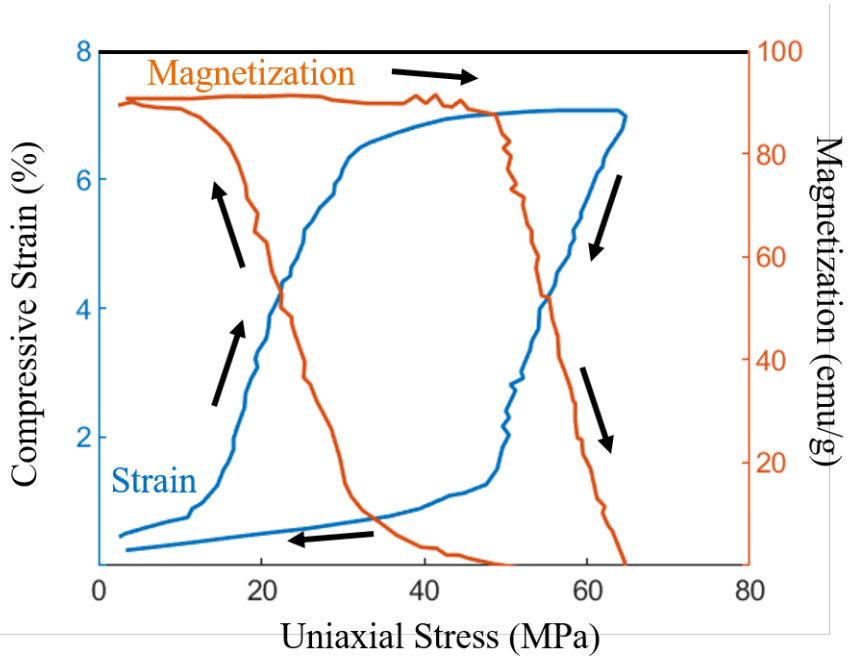

Figure 1.2: The magnetization of magnetic shape memory alloy NiCoMnIn under a 1T magnetic field is coupled with stress and strain. As stress and strain increase, the magnetization of NiCoMnIn substantially decreases [39]

1.4 Magnetic Sensing via Magnetic Shape Memory Alloys

Non-destructive evaluation requires a means of determining the internal state of a structure via external means. Magnetic sensing using embedded MSMA forms may be especially feasible in civil engineering structures since the magnetic permeability of concrete, water, and air are nearly identical to that of free space. For example, they have no noticeable effect on the magnetic field generated by a permanent magnet, while higher magnetic permeability materials like MSMAs will clearly alter a magneto-static field. Many MSMAs exhibit ferromagnetic behavior, and the most commonly studied is NiMnGa [27, 31]. Other ferromagnetic shape memory alloys, such as FeMnAlNi (FMAN), have the strength required to provide structural reinforcement and exhibit large recoverable pseudoelastic strains, have lower material costs, and are easier to process, given their higher ductility than traditional SMAs [40, 41]. FeMnAlNi has also been produced with large grains which can span the entire cross-section of small wires, though the material is typically more susceptible to failure at these grain boundaries [42, 43] and reliant on the individual crystal orientations [44]. The permeability of an MSMA can be correlated to material phase transformations, which themselves are driven by stress and temperature changes [39, 45, 46].

Since increases in stress can lead to stress-induced martensite (SIM) in an SMA, and since stress increases near a crack tip under external tensile loading [47, 48, 49], the presence of an internal crack in a host material can provoke the aforementioned magneto-mechanical (i.e. change in magnetic permeability) response in embedded MSMA components near such cracks. The stress fields and crack propagation behaviors in concrete materials have been further evaluated through various methods [50, 51, 16] that focus on mixed mode fracture in cement concrete and characterize the brittle fracture mechanics through both theoretical and experimental methods. The substantial localization of stress concentrations around a crack tip offers the potential to pinpoint crack tip locations. Studies have been performed to computationally correlate embedded SMA particle phase transformations with stress fields in a host [52, 53, 54], and robust models for SMAs exist to calculate the phase transformation in a finite element framework [55, 56, 57].

However, magnetic sensing in concrete structures using MSMAs has not been studied to date, and no method for external non-destructive evaluation of the type proposed has been investigated. This simultaneous use of MSMA components as magnetic sensors for non-destructive evaluation of failure and as structural reinforcement components represents an inherently multidisciplinary research effort with respect to both the computational and experimental domains. The analysis of phase transforming wires or rods embedded in a concrete structure for the manipulation of a magnetic signal requires a strong understanding of the solid mechanics of the concrete/wire interface, the use of external magnetic sensing (and thus related work with metrology sensitivities, probe placement, and specimen size), and the ability to interpret magnetic signals as internal stress fields. Therefore, computational studies are needed to explore the effectiveness of MSMAs for external magnetic sensing.

1.5 Thesis Summary

This work presents and evaluates such a computational framework to investigate the use of MSMA wires for SHM of concrete structures toward internal crack detection. An evaluation of the MSMA wire phase transformation near an embedded crack under three-point bend loading conditions is conducted using finite element analysis, coupled with a user material subroutine developed by Lagoudas, Hartl, and coworkers [57] to simulate the wire transformation from austenite to SIM. The spatially varying phase fractions associated with the resulting transformation are then mapped to a heterogeneous material permeability field that is input into a magnetostatic study considering the existence of a permanent magnet. Any MSMA magneto-mechanical response to a stress field generated near the tip of a crack in a host material provides a local alteration in the imposed magnetic field near an internal crack, enabling the potential to utilize external magnetic sensing for the detection of internal cracks and corresponding stress concentrations. The change in the resulting magnetic field near the SIM is then calculated, demonstrating for the first time the effectiveness of embedded MSMAs for internal crack detection. The results both support the feasibility of magnetic sensing by providing the means of correlating external

magnetic field changes with the presence of internal cracks and the location of SIM formed in embedded MSMA wires.

1.6 Thesis Outline

The structure of the thesis is laid out as follows:

- Chapter 2 provides a overview of the mathematical and computational tools employed in the work. This includes damage modeling methods, material calibrations, necessary constitutive relations, and the employment of finite element methods to the boundary value problems defined for each computational method.

- Chapter 3 describes the magneto-static modeling techniques and efforts to define a concrete-MSMA composite block undergoing damage. The changes in mechanical and magneto-static properties in the presence of loading beyond internal damage are evaluated in the finite element models. The effect of MSMA phase transformation on the magneto-static field is quantitatively determined for a defined feasible boundary value problem. External magnetic evaluation methods are described and their effectiveness is compared to conventional magnetic sensing methods.

- Chapter 4 explores expanded applications beyond a single MSMA wire embedded in a concrete block in the magneto-static domain. Large grain MSMA wires are modeled to define individual (and thus local) grain transformations, with the effects of these strain-driven phase transformations on external magnetic sensing capabilities quantified. MSMA cables are also explored in conjunction with the previous work with the single wire model, with the magnetic responses compared to the original form factor.

- Chapter 5 explores the use of transforming MSMA particles in an aluminum host for structural health monitoring applications. Multiple permeability modeling techniques are explored, and the effects of local particle phase transformation on the magneto-static field are

evaluated. The change in the magnetic field due to both the added presence of MSMA particles and their subsequent austenite to martensite phase transformation is explored, with the changes compared to the sensitivities of traditional magnetic sensors.

- Chapter 6 will summarize the work of this thesis, the results of the computational modeling, and future work in this field.

2. OVERVIEW OF COMPUTATIONAL ENGINEERING TOOLS

2.1 Simulation of the crack propagation

2.1.1 Structural Boundary Value Problem

The primary motivation of structural health monitoring (SHM) is the continuous evaluation of the state of a structure with respect to damage and degradation. In large scale civil infrastructure, particularly under cyclical loading, a common cause of structural damage is the formation and propagation of internal cracks. Thus, the modeling of such cracks and subsequent propagation is necessary to simulate internal damage.

The governing equations of the structural boundary value problem for a crack in a body are given as:

$$\nabla \bullet \boldsymbol{\sigma} + \mathbf{b} = \mathbf{0} \tag{2.1}$$

over the entire body Ω,

$$\boldsymbol{\sigma} \bullet \mathbf{n} = \mathbf{t} \tag{2.2}$$

over the surface under traction Γ_t, and

$$\boldsymbol{\sigma} \bullet \mathbf{n} = \mathbf{0} \tag{2.3}$$

over the surfaces of the crack faces Γ_c, where $\mathbf{n}$ is the unit outward normal vector, σ is the Cauchy stress, and $\mathbf{b}$ is an externally applied body force [58]. The surfaces of crack faces are considered traction free.

Hooke's law defines the constitutive relation as:

$$\boldsymbol{\sigma} = \mathbf{C} : \boldsymbol{\epsilon}, \tag{2.4}$$

where $\mathbf{C}$ is the stiffness tensor and ϵ is the strain tensor, defined as:

$$\boldsymbol{\epsilon} = \frac{1}{2}(\nabla \mathbf{u} + (\nabla \mathbf{u})^{\mathbf{T}}). \tag{2.5}$$

2.1.2 Linear Elastic Fracture Mechanics

The mechanics of the crack growth and stress field are based on linear elastic fracture mechanics (LEFM) [49]. The structural loading in question can be treated as Mode I fracture. The Westergaard Solution for the crack tip stress field under this failure mode is given by:

$$\sigma_{rr} = \frac{K_I}{\sqrt{2\pi r}}[\frac{5}{4}\cos(\frac{\theta}{2}) - \frac{1}{4}\cos\frac{3\theta}{2}], \tag{2.6}$$

$$\sigma_{\theta\theta} = \frac{K_I}{\sqrt{2\pi r}}[\frac{3}{4}\cos(\frac{\theta}{2}) + \frac{1}{4}\cos\frac{3\theta}{2}], \tag{2.7}$$

$$\sigma_{r\theta} = \frac{K_I}{\sqrt{2\pi r}}[\frac{1}{4}\sin(\frac{\theta}{2}) + \frac{1}{4}\sin\frac{3\theta}{2}]. \tag{2.8}$$

Here, K_I is the Mode I loading stress intensity factor, which can be obtained by solving the boundary value problem under specified geometry and boundary conditions. The stress intensity factor at fracture, K_I, can be determined using the energy required for fracture G and the Young's Modulus E as given in the following equation:

$$\frac{{K_{IC}}^2}{E} = G \tag{2.9}$$

The damage in the concrete is calculated and propagated using XFEM, the stress fields shown above, and the maximum principal stress and fracture energy to simulate the traction-separation response using a scalar damage parameter D as shown in Fig. 2.1 [59].

For a pre-existing crack in a finite element framework, the nodes surrounding the crack are prescribed with the Jump function as boundary conditions. Fig. 2.2 shows an example of the damage parameter D from Fig. 2.1 in the affected finite elements as implemented in ABAQUS,

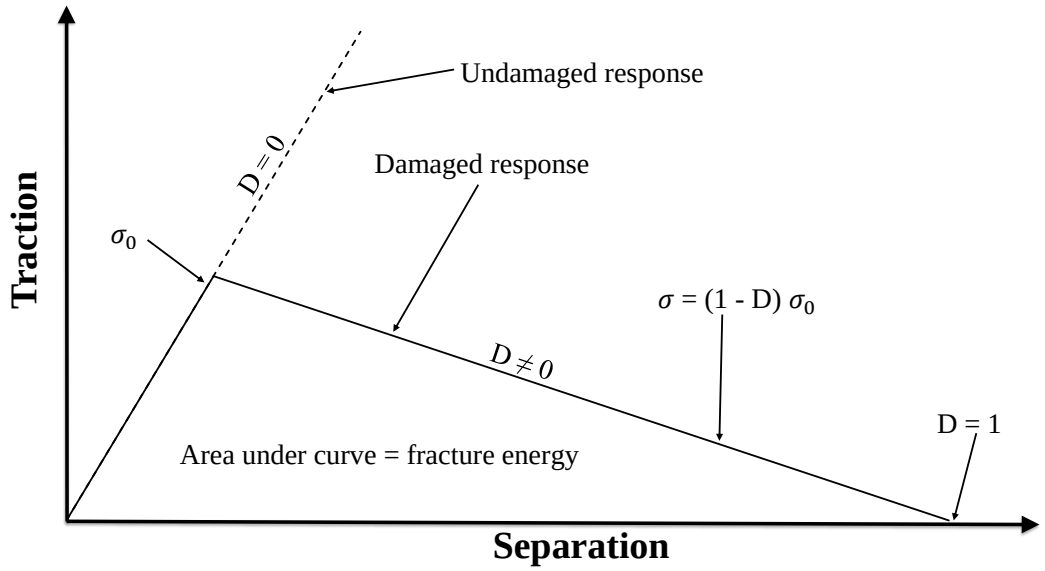

Figure 2.1: The calculation of damage and fracture uses a cohesive zone model, as shown in this traction-displacement curve. Given increasing separation, traction increases until a specified threshold is met, at which point the damage parameter D and fracture energy determine the decrease in traction before complete separation at $D = 1$. [59]

a finite element solver [60].

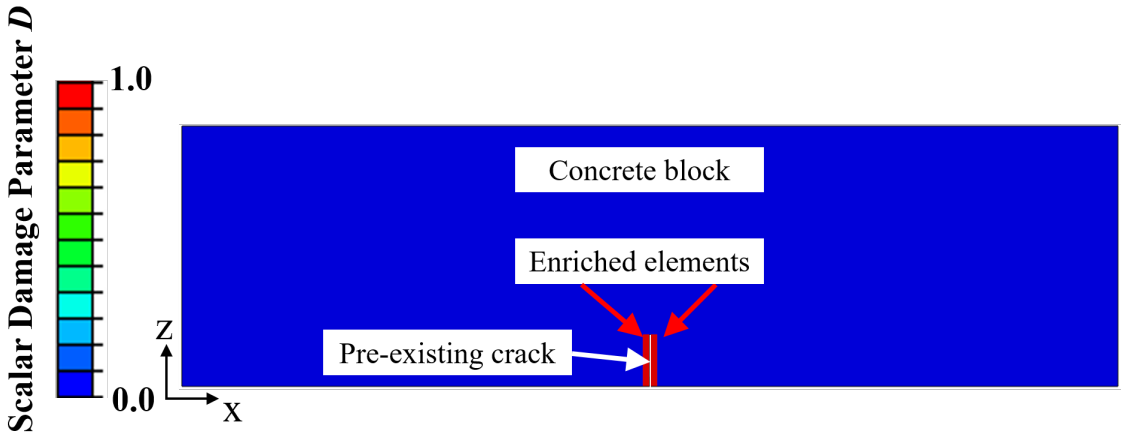

Figure 2.2: A pre-existing crack is defined as a surface which passes through a mesh. The nodes of the surrounding elements are enhanced using an extended finite element method.

2.1.3 Extended Finite Element Method

Modeling discontinuities such as cracks in a typical finite element framework requires a highly refined mesh near the discontinuities, which may hinder convergence, increase computational costs, and influence the solution. These limitations are more critical when considering the propagation of a crack due to the local crack tip field, which may require re-meshing as time-varying discontinuities change the geometry of the finite element model. A solution to ease the convergence and mesh requirements for such discontinuities is the extended finite element method (XFEM), which is available in Abaqus [60]. XFEM, as developed by Belytschko and co-workers [61, 62, 63], is a finite element method developed to characterize elastic crack growth without re-meshing using discontinuous enrichment functions added to the finite element framework to account for the presence of an asymptotic crack tip field. For a crack located on the original nodes, a crack can be modeled and meshed as seen in Fig. 2.3 [58]. The displacement is given by:

$$\mathbf{u^h} = \sum_{\mathbf{i=1}}^{\mathbf{n}} \mathbf{u_i} \phi_\mathbf{i}, \tag{2.10}$$

where $\mathbf{u_i}$ is the displacement for a given node i and ϕ_i is the associated shape function for each node i.

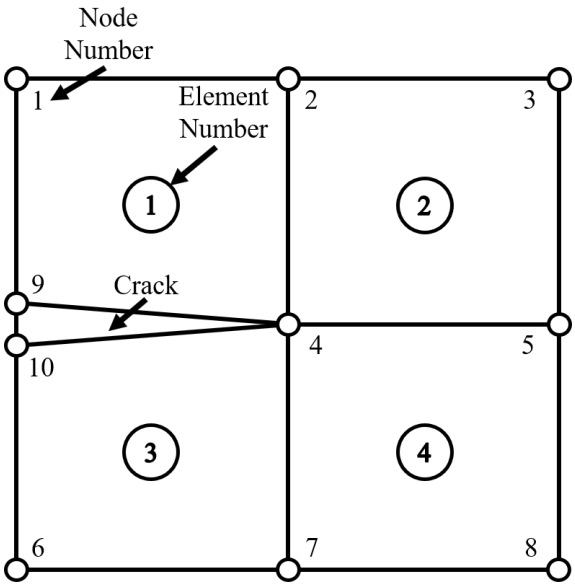

Figure 2.3: Finite element nodal array around a crack tip defined by mesh nodes

The finite element approximation accounting for this enrichment function is given as [61, 52, 58]:

$$u^h(\mathbf{x}) = \sum_{i=1}^{n} N_i(\mathbf{x})(u_i + \sum_{j=1}^{n_E} a_{ji} H(\mathbf{x})(r,\theta)), \tag{2.11}$$

where (r,θ) are components of the polar coordinate system with an origin at the crack tip and $N_i(X)$ are the standard continuous finite element shape functions. The quantity u_h represents the nodal displacements, and a_{ji} are the enrichment function coefficients, of which there are n_e. This method allows for crack growth without re-meshing as the crack propagates and the requisite crack tip mesh refinement that accompanies the traditional crack tip finite element methods. $H(\mathbf{x})$ is the Heaviside (or Jump) function associated with the discontinuities along the crack surface

given as:

$$H(x) = \left\{ \begin{array}{ll} 1, & if(\mathbf{x} - \mathbf{x}^*) \bullet n \geq 0 \\ -1, & if(\mathbf{x} - \mathbf{x}^*) \bullet n \leq 0 \end{array} \right\}, \tag{2.12}$$

where **x** is any point, x^* is the point on the crack surface closest to X, and n is the normal unit vector outward on the crack surface.

Clearly, an advancing crack will not always align itself with the nodes of a finite element mesh. Thus, there must exist a differentiation between elements which are enriched with a function to account for a crack face (and thus a traction-free surface) and element with a crack tip field. Nodes on elements bisected by a crack use the "Jump" function H, while elements with a crack tip use a crack tip field enrichment function. An example mesh can be seen in Fig. 2.4.

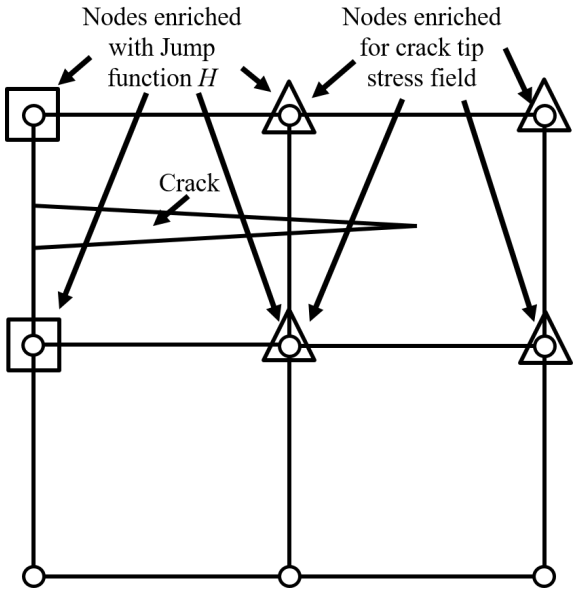

Figure 2.4: Finite element nodal array adds an enrichment function H for discontinuities (nodes in squares) and an enrichment function for the crack tip stress field (nodes in triangles)

This complete enrichment function is defined by Moes, Dolbow, and Belytschko [58, 61] as:

$$\mathbf{u^h} = \sum_{\mathbf{i}\in\mathbf{I}} \mathbf{u_i}\phi_\mathbf{i} + \sum_{\mathbf{j}\in\mathbf{J}} \mathbf{u_j}\phi_\mathbf{j}\mathbf{H}(\mathbf{x}) + \sum_{\mathbf{k}\in\mathbf{K}} \phi_\mathbf{k}(\sum_{\mathbf{l=1}}^{\mathbf{4}} \mathbf{c_k^l}\mathbf{F_l}(\mathbf{x})) \tag{2.13}$$

in which J represents the set of all nodes on elements bisected by a crack, and K represents all the nodes of elements containing a crack tip. The functions $F_l(\mathbf{x})$ are defined by:

$$F_l(r,\theta) \equiv \sqrt{r}\sin(\frac{\theta}{2}), \sqrt{r}\cos(\frac{\theta}{2}), \sqrt{r}\sin(\frac{\theta}{2})\sin(\theta), \sqrt{r}\cos(\frac{\theta}{2})\sin(\theta) \tag{2.14}$$

2.2 Experimental Parameters Required to Model Damage Evolution

2.2.1 Mechanical Properties of a Concrete Mortar Specimen

The mechanical properties of the concrete mortar specimen were determined using a displacement-controlled three-point bend test [64] with deflection measurements on both the top and bottom face of the specimen as shown in Fig. 2.5. The concrete mortar specimens were cast with a water to cement ratio of 0.4 and cured for seven days at room temperature before testing. The mechanical fracture properties of the concrete mortar to be determined and used in a structural model are listed henceforth. The geometric parameters L, b, d, and h are span length between supports, span width, specimen depth, and specimen height, respectively. The material parameters E_{conc}, θ_t, and G are measured Young's modulus, tensile strength, and fracture energy, respectively. The maximum loading and deflection at failure are P and δ, respectively. The Poisson ratio ν used in the model is taken from previous concrete experimental work in the literature [65]. An experimental three-point bend test was conducted on the mortar block setup shown in Fig. 2.5.

The three-point bend test results were then used to determine these mechanical properties using the relations shown in Fig. 2.1 and ASTM concrete testing standards [64] The Young's modulus E_{conc} is given by, at the point of fracture:

$$E_{conc} = \frac{\sigma}{\epsilon} = \frac{L^3 P}{4bd^4}. \tag{2.15}$$

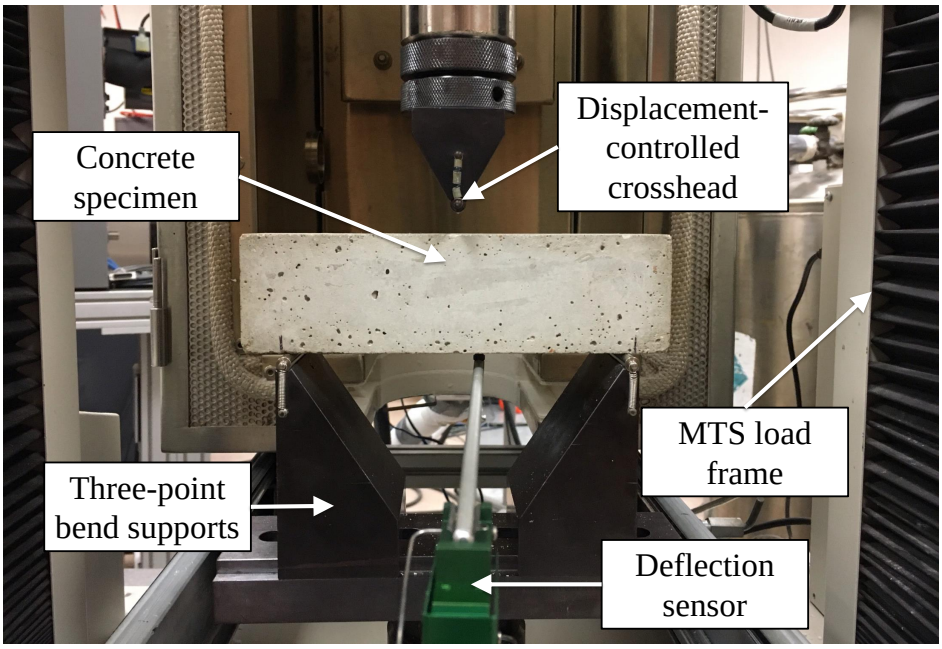

Figure 2.5: Three-point bend test of an un-cracked concrete specimen without an embedded wire; results were used to calculate the maximum tensile stress, Young's modulus, and fracture energy of the concrete.

The modulus of rupture R, the measure of a material's strength before rupture, is given by:

$$R = \frac{3PL}{2bd^2}. \tag{2.16}$$

With the Young's modulus and modulus of rupture R determined, the critical tensile strain ϵ_t must be:

$$\epsilon_t = \frac{6\delta d}{L^2}. \tag{2.17}$$

The total fracture energy G before failure is given by:

$$G = \frac{\sigma_t \delta}{2} = \frac{3PL\delta}{4wd^2}. \tag{2.18}$$

Both a pure concrete specimen and a concrete specimen with three embedded wires were

Table 2.1: Concrete testing properties and parameters

PROPERTY	VALUE
(Concrete testing properties)	
E_{conc}	4.86 GPa
ν	0.18
R	2.7 MPa
G	0.08 N/mm
(Specimen Geometric Properties)	
L	150 mm
b, d	50 mm

subject to the three-point bend test described previously. The concrete material properties were determined via the three-point bend test of the pure concrete specimen, while the benefits of embedding three wires in the specimen can be clearly seen in Fig. 2.6 The addition of embedded wires in the concrete specimen leads to an increase in the both specimen strength and fracture energy.

The cohesive zone model was used to model the interactions between the MSMA wire and the concrete host. The properties for the cohesive zone were taken from a pullout test in which an MSMA wire was pulled out of a concrete block as shown in Fig. 2.7, and the properties of the cohesive zone can be found in Table 2.2.

2.3 Shape Memory Alloy Constitutive Modeling

A detailed description of the constitutive thermomechanical response can be found elsewhere [57], while a succinct description of the model for this material behavior is provided here. The thermomechanical model utilized is a three-dimensional constitutive model of Lagoudas et al. [57], which extends the model originally proposed by Boyd and Lagoudas [56]. In summary, the total infinitesimal strain of an SMA material point at constant temperature is the summation

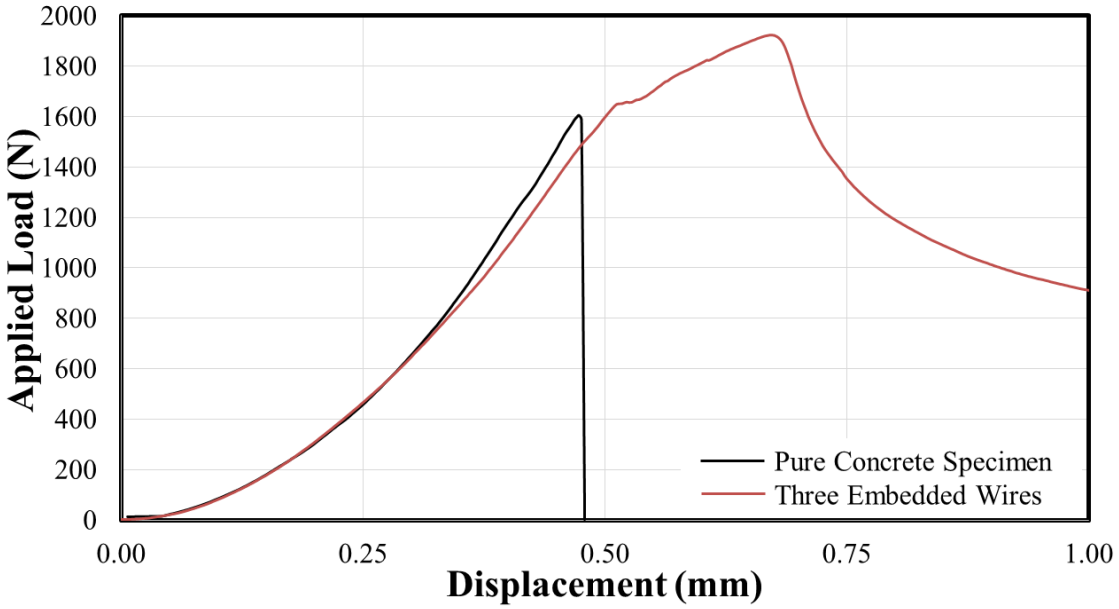

Figure 2.6: The addition of embedded wires in a concrete specimen leads to an increase in strength and fracture energy.

Table 2.2: Cohesive Zone Properties

PROPERTY	DESCRIPTION	VALUE
σ_{max}	Maximum Principal Stress	9.5 MPa
G_{cz}	Cohesive zone fracture energy	0.03 N/mm
σ_{cz}	Cohesive Zone Maximum Principal Stress	0.5 MPa

of the elastic strain $\boldsymbol{\varepsilon^e}$ and the transformation strain $\boldsymbol{\varepsilon^t}$ as shown below:

$$\boldsymbol{\varepsilon} = \boldsymbol{\varepsilon^t} + \boldsymbol{\varepsilon^e}. \tag{2.19}$$

The transformation strain tensor $\boldsymbol{\varepsilon^t}$ is the inelastic strain generated during transformation from austenite to martensite and subsequently recovered during full reverse transformation. The

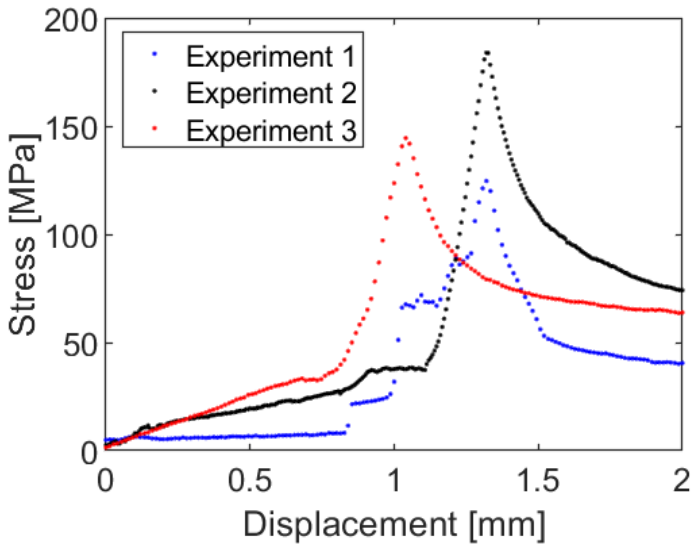

Figure 2.7: Experimental test of cohesive properties between an embedded MSMA wire and a concrete host. The material properties were determined by the traction-separation curve parameters in section 2.1.2.

change from austenite to martensite is quantified by the martensite volume fraction ξ, which accounts for the sum of all martensitic variants and is bounded from zero to one, such that:

$$0 \leq \xi \leq 1. \tag{2.20}$$

For a constant temperature, which will be assumed throughout the work, the coupling of stress and strain is given by

$$\boldsymbol{\varepsilon} = \boldsymbol{S}(\xi)\boldsymbol{\sigma} + \boldsymbol{\varepsilon^t} \tag{2.21}$$

where $\boldsymbol{S}(\xi)$ is a fourth-order compliance tensor dependent on the martensite volume fraction. A strict relationship exists between the time rate of change of the transformation strain and martensitic volume fraction that quantifies the extent of martensite transformation, such that [57]:

$$\dot{\boldsymbol{\varepsilon^t}} = \boldsymbol{\Lambda^t}\dot{\xi},\ \dot{\boldsymbol{\varepsilon}} > 0, \tag{2.22}$$

where $\mathbf{\Lambda^t}$ is the transformation direction tensor during forward (austenite to martensite) transformation, as will be considered here. $\mathbf{\Lambda^t}$ is given by:

$$\mathbf{\Lambda^t} = \frac{3}{2} H \frac{\boldsymbol{\sigma}'}{\bar{\sigma}}. \tag{2.23}$$

This follows from an assumption that the application temperature is such that reverse transformation is not possible (i.e. $T > M_s$). In Eq. 2.23, H represents the maximum transformation strain magnitude generated during full transformation from austenite to martensite, assumed constant in this study. The Von Mises stress $\bar{\sigma}$ is given by:

$$\overline{\sigma} = \sqrt{\frac{3}{2} \boldsymbol{\sigma}' : \boldsymbol{\sigma}'}, \tag{2.24}$$

where $\boldsymbol{\sigma}'$ is the deviatoric component of the stress tensor $\boldsymbol{\sigma}$.

The forward transformation criterion (representing forward transformation initiation and propagation when ${\Phi^t}_{fwd} = 0$) is given by:

$${\Phi^t}_{fwd}(\boldsymbol{\sigma}, T, \xi) = H\overline{\sigma} + p(\xi, T) - Y_0 = 0, \dot{\xi} > 0, \tag{2.25}$$

where Y_0 is the critical thermodynamic driving force to initiate and sustain forward transformation and $p(\xi, T)$ is a thermodynamic function capturing both hardening and temperature dependency for forward transformation.

The specific material properties used to calibrate the transformation criteria within the model include M_s, M_f, A_s, A_f, known as martensitic start, martensitic finish, austenitic start and austenitic finish temperatures at zero stress level, respectively, and C^A and C^M (the stress influence coefficients for austenite and martensite). The maximum transformation strain, and YoungâĂŹs modulus, PoissonâĂŹs ratio, and coefficient of the thermal expansion in both austenite and martensite phases (H, E^A, E^M, ν^A, ν^M, α^A,α^M) are also needed for calibration and are obtained through the experimental calibration process as outlined in detail in [57].

The phase transformation from austenite to martensite also changes the magnetic properties of an MSMA. This effect will be exploited in this work, and will be modeled by considering the change in magnetic permeability of austenite and martensite, where a linear relationship between permeability and martensite volume fraction will be assumed such that:

$$\mu_m(\xi(\mathbf{X})) = \mu_A - (\mu_A - \mu_M)\xi(\mathbf{X}), \tag{2.26}$$

where μ_m, μ_A, and μ_M represent the permeabilities of an MSMA in a mixed phase, in pure austenite, and in pure martensite, respectively. This relationship is called the linear rule of mixtures, and will be mentioned later when comparing methods of modeling effective magnetic permeabilities.

FeMnAlNi is a magnetic SMA chosen for both its magnetic and structural qualities, and given the motivations of this work, the low cost of its constituents. Through specific heat treatment and crystal orientations investigated by Tseng et al [40, 66, 67], FeMnAlNi wires with large grain sizes have been created that exhibit the material properties shown in Table 2.3 [1]. Notably, the stress-influence coefficients, at 0.74 MPa/K, are significantly lower than typical SMAs (e.g., usually 7-10 MPa/K) [57]. This property is ideal for stress-driven sensors embedded into civil infrastructure in that lower stress influence coefficients quantify a weakened influence of the unavoidable temperature changes (e.g., due to time and seasonal effects) on the phase transformation (and thus sensory) response of the embedded MSMA components.

2.4 Magneto-Static Modeling

The magnetic sensing is evaluated and simulated using the COMSOL magneto-statics implementation of the finite element method [68]. The developed model demonstrates the sensing capabilities of an external magnet paired with a sensor detecting an internal magnetization change in the MSMA wire, specifically by considering the change in magnetic flux predicted in the region occupied by the sensor. The magneto-static study utilizes Ampere's law with the assumption

Table 2.3: SMA material properties for FeMnAlNi [1].

PROPERTY	VALUE
(Elastic Properties)	
E_A, E_M	106 GPa, 141 GPa
$\nu_A = \nu_M$	0.33
(Phase Diagram Properties)	
M_s, M_f	243 K, 182 K
A_s, A_f	193 K, 260 K
$C^A = C^M$	0.74 MPa/K
(Transformation Strain Properties)	
$H = H_v$	6.7%

that no external currents are applied to solve for the magnetic flux density B:

$$\oint \boldsymbol{B} \bullet d\boldsymbol{l} = \mu_0 I. \tag{2.27}$$

where l defines any enclosed loop through which magnetic flux density B passes, μ_0 is the magnetic permeability of free space (1.257e-6 H/m), and I is the current enclosed by loop l.

Due to the static, steady-state nature of the model and lack of a current source, the previous equation simplifies to

$$\oint \boldsymbol{B} \bullet d\boldsymbol{l} = 0. \tag{2.28}$$

Locally, this is expressed by

$$\nabla \bullet \boldsymbol{B} = -\nabla \bullet (\mu_0 \nabla \boldsymbol{\phi_m} - \mu_0 \boldsymbol{M}) = 0. \tag{2.29}$$

where $\boldsymbol{\phi_m}$ is the magnetic flux potential.

In linearly magnetizable materials, the magnetic field strength $\boldsymbol{H}$ is related to the magnetic flux density $\boldsymbol{B}$ and the magnetization field $\boldsymbol{M}$ by

$$\boldsymbol{H} = \boldsymbol{B}/\mu_0 - \boldsymbol{M} = \boldsymbol{B}/\mu_m, \tag{2.30}$$

where μ_m is the material's magnetic permeability.

The MSMA wire has locally variable magnetic permeability μ_m driven by changes in the martensite volume fraction ξ, this then being driven by the changing local stress field. This will alter any external magnetic field strength $\boldsymbol{H}$ in the vicinity of a stressed MSMA wire given a fixed source field, such as from a permanent magnet.

2.5 Measuring Magnetic Field Strength in a Magneto-Static Solution

After solving a prescribed magneto-static boundary value problem, external sensing is simulated by calculating changes in the magnetic field due to internal damage. Magnetic field strength is defined either by the magnetic field strength H or the magnetic flux density B. As previously described in section 2.4, B is related to H by the local material permeability. Hall probes are a common commercially available sensor for measuring the magnetic flux density B by taking advantage of the Hall effect. The Hall effect states that in the presence of an applied magnetic field B, when an applied electric current I passes through a conductor the magnetic field exerts a transverse force on the electrons in the applied current. The electrons will build up on one side of the conductor, creating a measurable voltage change which can be correlated to the magnetic flux density normal to the conductor. The magnetic force created by the Hall effect F_m is:

$$F_m = ev_dB \tag{2.31}$$

where e and v_d represent the charge of an electron and the electron drift velocity, respectively. The voltage across a Hall probe is given by:

$$V_H = \frac{IB}{ned} \tag{2.32}$$

where n is the density of charge carriers and d is the thickness of the conductor in the Hall probe. Thus, the normal magnetic flux density through a surface (or a single point with a defined normal direction) can be measured using existing sensory technology.

2.6 Modeling of Magnetic Permeabilities in Composite Structures

2.6.1 Effective Medium Approximations in Composites

The magnetic permeability of a two-material composite can be treated macroscopically as a single composite material for smaller material inclusions evenly dispersed in a host matrix. This is applicable for small MSMA components embedded in a larger material matrix. The macroscopic magnetic properties for such a composite can be modeled using effective medium approximations (EMA) for composites. As a magnetic inclusion is magnetized, the average quasi-static magnetic field inside the MSMA depends on the local magnetic polarization P [69]:

$$P(n, \mu_i, \mu_h) = \frac{\mu_i - \mu_h}{\mu_h + n(\mu_i - \mu_h)}, \tag{2.33}$$

where n, μ_i, and μ_h are the inclusion shape factor, inclusion magnetic permeability, and host magnetic material permeability. Each magnetic permeability μ can be expanded as a relative magnetic permeability multiplied by the magnetic permeability of free space as $\mu_m = \mu_r \mu_0$, and a simplification leads to the removal of μ_0. Thus, all work on composite magnetic permeabilities can be computed using the material relative magnetic permeabilities in place of the true magnetic permeabilities. It is also worth noting that the relation for electric polarization has the exact same format and shape factor as that in Eq. 2.33, except with electrical permittivities in place of the magnetic permeabilities.

2.6.2 Maxwell Garnett Approximation

The primary EMA used for materials in a host matrix is the Maxwell Garnett approximation (MGA), which derives directly from the Lorentz dipole field equations for charged particles in a vacuum. MGA assumes the interactions between inclusions between inhomogeneities to be negligible. By defining the local magnetic field of a series of particles in a host material instead of a vacuum, the magnetic permeability of a homogeneous region with, on average, evenly dispersed spherical inclusions can be approximated by the following equation:

$$\mu_e = \mu_h \frac{\mu_h + \frac{1+2p}{3}(\mu_i - \mu_h)}{\mu_h + \frac{1-p}{3}(\mu_i - \mu_h)}, \tag{2.34}$$

where μ_e represents the effective magnetic permeability of the composite and p represents the volume fraction of the particle inclusions. For a single material this approximation can be rearranged for this n material as such:

$$\frac{\mu_e - \mu_h}{\mu_e + 2\mu_h} = p\frac{\mu_n - \mu_h}{\mu_n + 2\mu_h}, \tag{2.35}$$

which for N different material inclusions is mathematically described as

$$\frac{\mu_e - \mu_h}{\mu_e + 2\mu_h} = \sum_{n=1}^{N} p_n \frac{\mu_n - \mu_h}{\mu_n + 2\mu_h}. \tag{2.36}$$

However, a limitation of Eq. 2.36 is the treatment of the host material magnetic permeability μ_h as compared to the permeability of small inclusions μ_i. While the inclusions can be summed up in any manner and produce the same mathematical solution, changing the definition of which material is the host material as compared to the inclusion materials will lead to multiple solutions. As the volume fraction increases, the inhomogeneity of interactions between inclusions will increase, meaning the assumption of these inhomogeneities as negligible may no longer be valid. Thus, MGA is only valid when the volume fractions of all inclusions and the host material are orders of magnitude different. An extension of MGA is needed to account for inclusion larger

volume fractions and the associated interactions between other inclusions.

2.6.3 The Landau-Lifshitz-Looyenga (LLL) Mixing Rule

The Landau-Lifshitz-Looyenga (LLL) mixing rule is a more rigorous EMA method extending the MGA via an iterative method of replacing material from a homogeneous component with a second component. Then, the bulk component material properties are calculated and the bulk material is treated as the new homogeneous component. Small portions of the material are added for each iteration, until the material concentrations of the bulk material are equal to the volume fraction of the inclusions. As such, the shape of the inclusions is not considered, and thus the LLL mixing rule can be expanded to general inclusions. The LLL mixing rule defines the effective magnetic permeability μ_e of a composite material by [70]:

$$\mu_e = (\mu_h + p((\mu_i)^{\frac{1}{3}} - (\mu_h)^{\frac{1}{3}}))^3 \tag{2.37}$$

where p represents the volume fraction of inclusions in the host matrix. These macroscopic relations allow for the treatment of small MSMA particle inclusions in a larger matrix to be mathematically modeled as a single homogeneous material.

2.6.4 Comparison of Magnetic Mixing Rules

Two options present themselves for modeling material magnetic permeability in a magnetostatic model: i) modeling each material individually with its own respective magnetic permeability or ii) modeling multiple material components as a single composite for increased efficiency. For materials with nearly identical magnetic permeabilities (i.e. air and concrete) both materials can be treated as a single domain and no further permeability calculations are required. For material domains with varying magnetic properties such as MSMA components with both martensitic and austenitic variants, the rule of mixtures will be used due to the lack of physical inclusions and the large spectrum of interactions occurring between regions with different magnetic properties. For composites consisting of multiple materials, the LLL mixing rule will be employed to approximate the magnetic permeability for a given region in the composite based on the average

permeabilities of both the host and the inclusions. The LLL mixing rule was chosen over the MGA because it is more robust in that it accounts for interactions between inclusions. Thus, the magneto-static modeling of composites is not limited to very small volume fractions of (MSMA) inclusions. For example, if partially-transformed MSMA particles are embedded in an aluminum host, first the rule of mixtures is used to determine the magnetic permeability of each MSMA particle (the aluminum host has a constant magnetic permeability regardless of loading). Next, one could either i) define the MSMA particles and the aluminum host as individual material domains in the magneto-static model or ii) treat the entire region as a unified domain with the magnetic properties of a single material as defined by the LLL mixing rule.

Fig. 2.8 shows an example of how magnetic relative permeability changes for a composite material with a unmagnetizable host material (i.e., having a relative magnetic permeability of 1) and the additions of a magnetizable material into the composite with a magnetic permeability of 16. The divergence between the LLL method and MGA after approximately a 5 percent volume fraction is due to the limitations of MGA as the volume fraction of the host and inclusions become comparable.

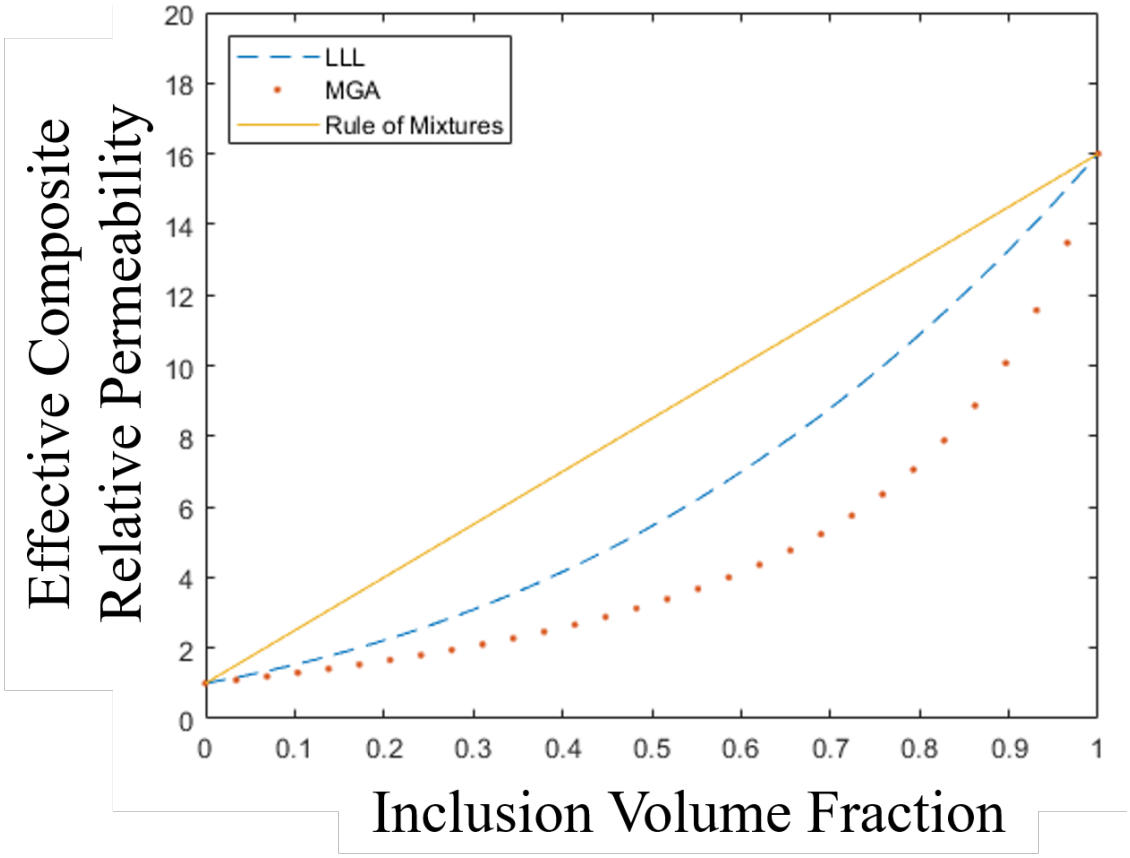

Figure 2.8: The effective material relative magnetic permeability for a unmagnetizable host an embedded material with a relative permeability of 16 increases with volume fraction of the inclusions. The MGA and LLL mixing rule are very similar when interactions between inclusions are insignificant (volume fractions below 0.05).

3. MAGNETIC SENSING OF LOCALLY TRANSFORMED MSMA WIRES EMBEDDED IN A CONCRETE MATRIX

Structural health monitoring using magnetic sensing requires evaluating local changes in a magnetic field to determine the changes in local damage state, and thus in the health, of a material or body. For this change in magnetic field to have sensory significance, it must be correlated to specific internal flaws or damage incurred. A robust computational framework to evaluate the structural mechanics of internal damage, the response of an embedded MSMA component in the vicinity of such damage, and the magnetic response of the system due to the change in magnetic permeability of the MSMA is required and is developed herein. Due to the different physical (and associated constitutive) responses required for evaluation, the computational framework is divided into two distinct models: i) a structural mechanics model to evaluate the mechanical effects of specified structural damage on an embedded MSMA and ii) a magneto-static model to evaluate the sensing capabilities of an external magnet and sensor combination in detecting the structural damage via the magneto-mechanical response of the MSMA.

3.1 Structural Modeling of MSMA Wire Phase Transformation

3.1.1 Structural Boundary Value Problem

As shown in Fig. 3.1, a concrete specimen under three-point bend loading is considered in this study to simulate the response of an embedded MSMA component due to stress concentrations imposed by a crack propagation through the concrete domain. The structural mechanics of the concrete-MSMA wire composite are modeled in ABAQUS [60], represented as a wire embedded in a concrete block under three-point bend loading conditions. The block is 180 mm by 50 mm by 50 mm and considers fixed load frame supports under the block spaced 150 mm apart. The MSMA wire has a 1 mm radius and is embedded 15 mm away from the bottom face of the concrete block. The dimensions can be seen in Table 3.1. The model considers a vertical (-z) load applied to the center of the top face of the concrete block, wherein damage initiates from the

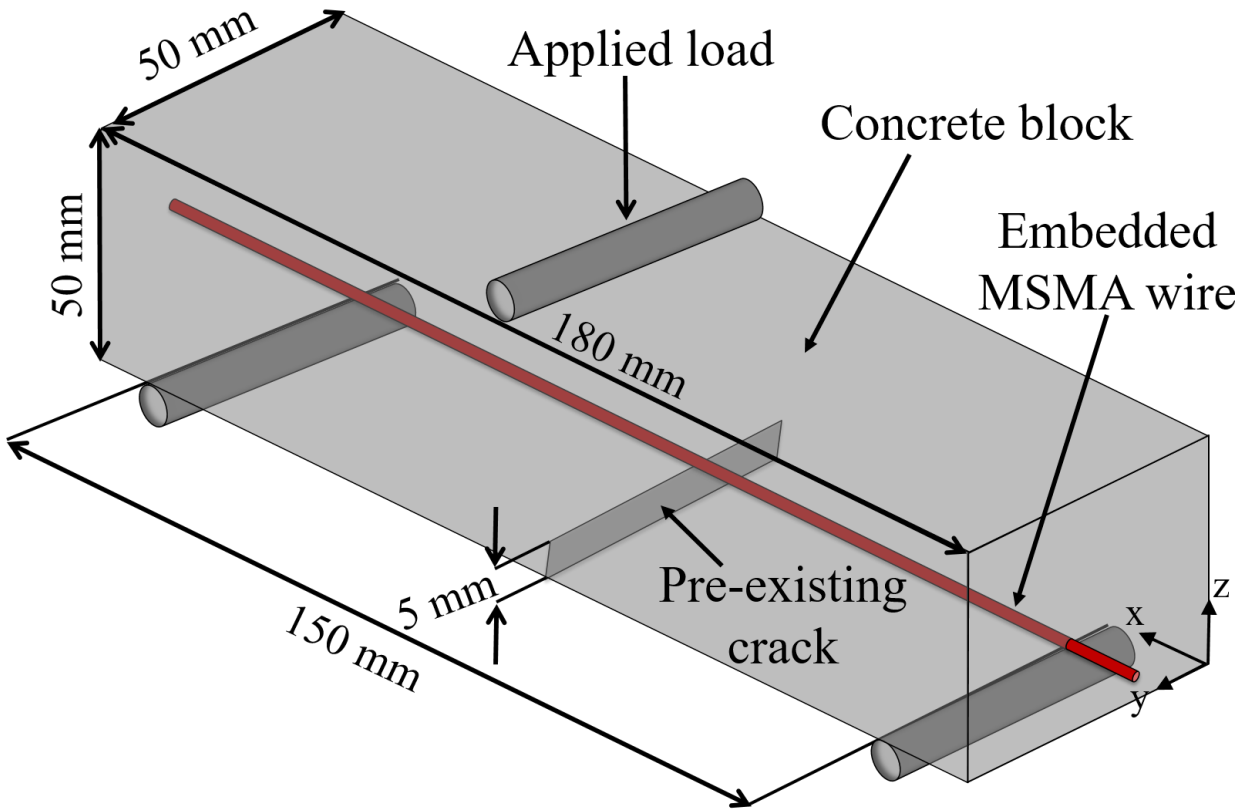

Figure 3.1: Structural mechanics model consists of a concrete block with a pre-existing crack and an embedded MSMA wire, subjected to three-point bending.

tip of a pre-existing crack of length 5 mm and propagates through the block towards the MSMA wire, creating a local stress concentration near the moving crack tip. As the crack tip stress field approaches the MSMA wire, the wire transforms locally over a finite region near this internal concrete damage. Initially, the entire model has a scalar damage parameter D of 0 (meaning no damage has accrued) except for the boundaries define by the pre-existing crack. This initial loading and damage parameter D as the crack tip advances can be seen in Fig. 3.2.

The regions neighboring the crack tip reach the stress required for damage initiation. The mode I crack tip stress field as seen in Fig. 3.3. This initial stress field follows the typical response of an edge crack under tensile loading as described by the Williams solution [49].

Table 3.1: Structural Model Parameters

PROPERTY	VALUE	DESCRIPTION
L_B	180 mm	Concrete Block Length
W	50 mm	Concrete Block Width
H	50 mm	Concrete Block Height
R_W	1 mm	MSMA Wire Radius
L_{crack}	5 mm	Pre-existing Crack Length
$D_{supports}$	150 mm	Distance Between Supports
W_Y	25 mm	MSMA Wire Y-Coordinate
W_Z	15 mm	MSMA Wire Z-Coordinate

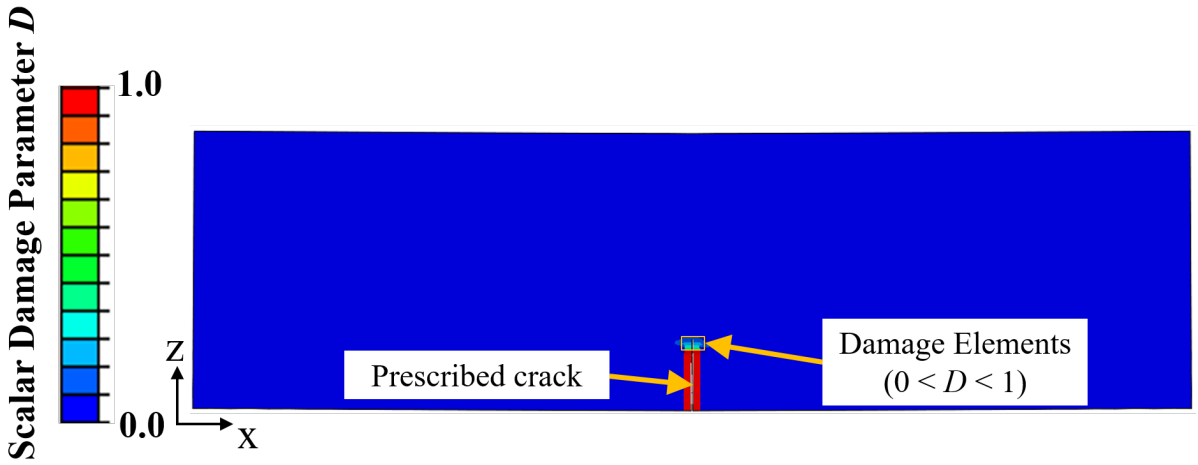

Figure 3.2: As the crack propagates through the concrete block, damage D increases from 0 to 1 before the crack propagates farther.

Fig. 3.4 illustrates the finite element results obtained by the XFEM approach for propagation of a crack through the concrete block with an embedded MSMA wire described earlier under 3-point bend conditions. The results show the propagating crack tip stress concentration and the subsequent loading of the MSMA wire lead to a phase transformation from austenite to SIM in the

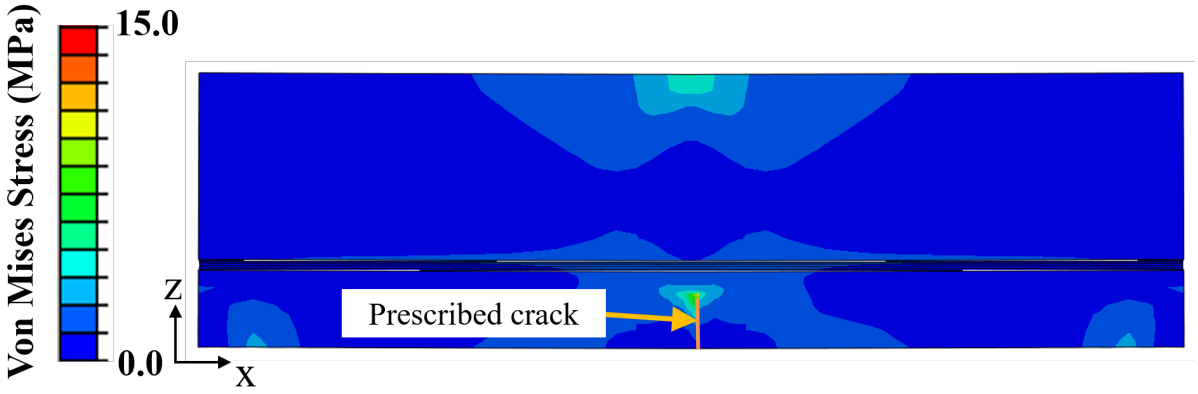

Figure 3.3: Crack tip field around a prescribed crack under 3-point bend loading before damage initiation.

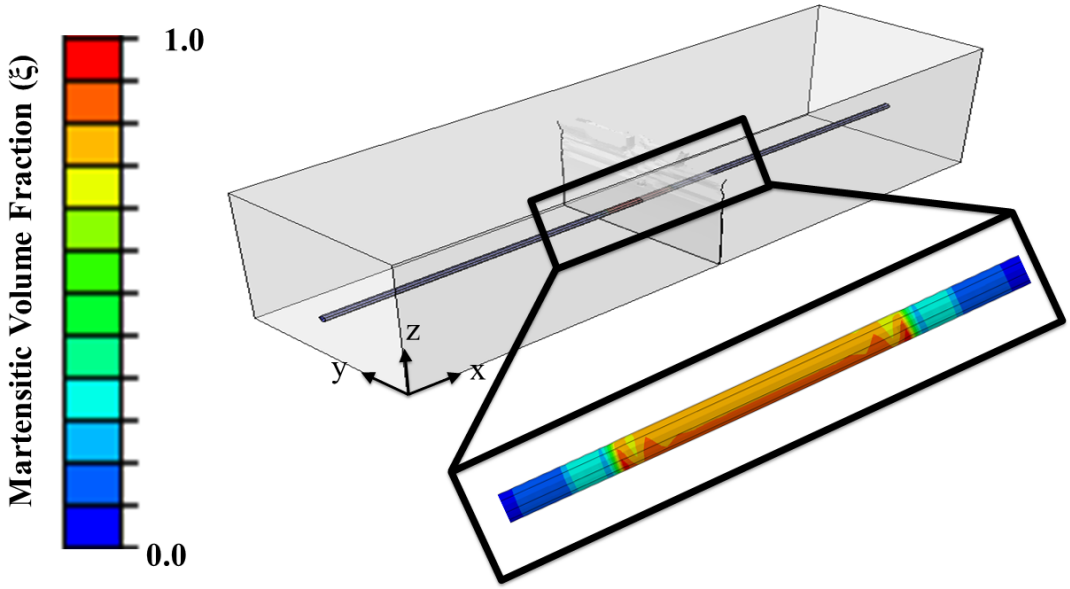

Figure 3.4: The martensitic volume fraction of the embedded MSMA wire increases around the crack tip propagating in concrete mortar domain.

central portion of the wire. The inhomogeneous magnetic permeability is then mapped $\mu_m(\mathbf{X}) = \mu_{\mathbf{m}}(\xi(\mathbf{X}))$ from the structural modeling results to the magneto-static model by considering the

average martensite volume fraction $\xi(\mathbf{X})$ of the wire along its length, the magnetic permeability values of austenite and martensite, μ_A and μ_M, and the linear rule of mixtures $\mu_m(\xi(\mathbf{X})) = \mu_{\mathbf{A}} - (\mu_{\mathbf{A}} - \mu_{\mathbf{M}})\xi(\mathbf{X})$.

3.1.2 Structural Model Validation

Tests were conducted to provide a comparison of computational results to experimental results for the structural finite element model. First, a concrete specimen was made with the dimensions of a 50 mm by 50 mm by 180 mm concrete block with an embedded 15 mm from the bottom of the block as previously described. The supports below the concrete block were located 15 mm away from the ends of the concrete block, a distance of 150 mm away from each other, the same as the computational model. Then a displacement-controlled 3-point bend test was conducted on the specimens, with the load and vertical displacement of the top of the block recorded. The 3-point bend test was then run on the structural FEA model through fracture with material properties given in Table 2.2. The experimental and computational results can be seen in Fig. 3.5. The difference in loading between the experimental and computational results is due to the surface roughness of the concrete specimen, which is crushed until the loading is sufficiently large enough to compact the inhomogeneities on the surface.

3.2 Description of the Magneto-Static Model

The magneto-static FEA model shown in Fig. 3.6 (following from the mechanics model of Fig.3.1) consists of an MSMA wire embedded in near one of the lateral faces of concrete block with a permanent magnet on the opposing lateral face of the concrete block for generating a static magnetic field. The concrete specimen considered in the magneto-static modeling is the same size as that considered in both the structural testing and modeling. The magnet has a radius of 6.35 mm and a length of 50.8 mm, and its performance is defined by its residual flux density of B_r = 1.3 T, fully aligned with the lower axis of the magnet and taken from the magnet used in material calibrations. It is a common residual flux density for commercial AlNiCo and Neodymium N42 magnets [71]. These geometric and magnetic parameters can be found in Table 3.2.

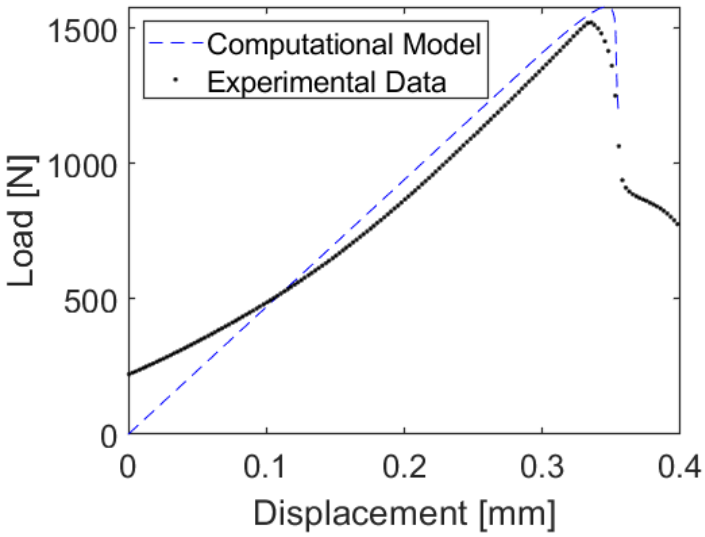

Figure 3.5: The results of a 3-point bend test on a concrete block with an embedded wire both through experimental and computational methods.

Table 3.2: Magneto-Static Model Parameters

PROPERTY	VALUE	DESCRIPTION
L_B	150 mm	Concrete Block Length
W	50 mm	Concrete Block Width
H	50 mm	Concrete Block Height
L_M	50.8 mm	Magnet Length
R_M	6.35 mm	Magnet Radius
B_r	1.3 T	Magnet Remanent Flux Density
R_W	1 mm	MSMA Wire Radius

All magneto-static evaluations are performed by measuring the magnetic flux density passing through a single point in the direction normal to the face of the magnet (-z). This is analogous to the use of Hall probes, which measure the normal magnetic flux density over a very small

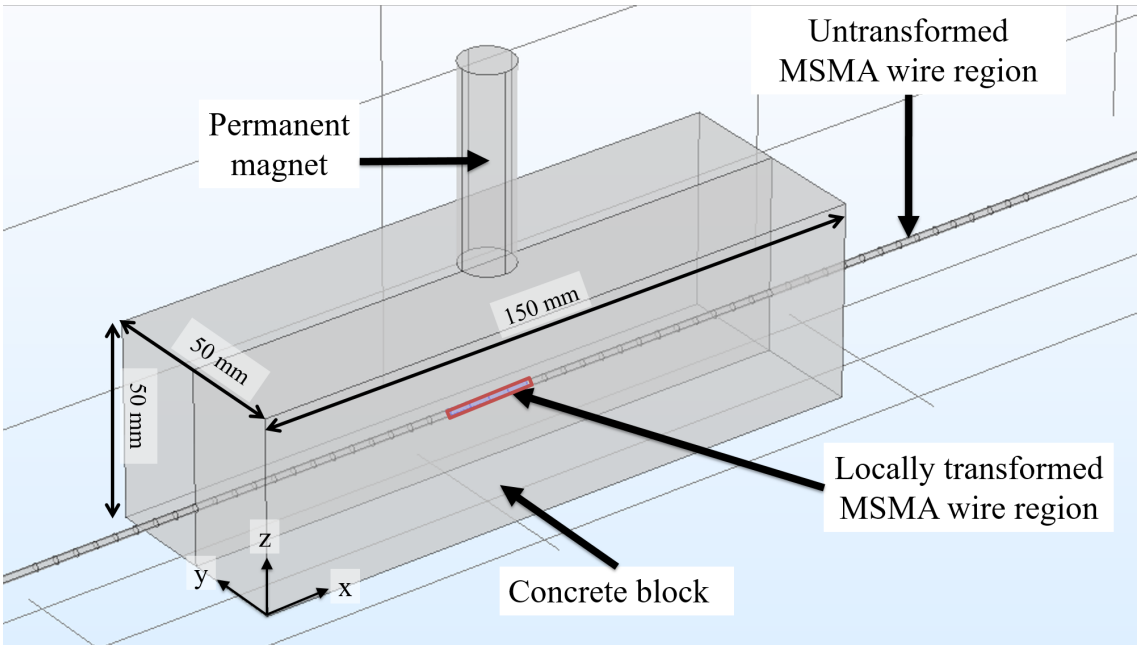

Figure 3.6: The magneto-static model consists of a segmented MSMA wire embedded in a concrete block with a magnet placed on one side of the block. The concrete has the same magnetic permeability as free space, thus it serves only visual and geometric purposes.

active area. An air domain encompassing the entire model is required for flux conservation, with size studies performed to ensure the domain is sufficiently large to prevent its boundary from influencing the results. The change in magnetic flux density due to transformation of a local region of the MSMA wire from austenite to martensite was measured as a function of the air domain radius, from 0.15 to 1.0 m. As seen in Fig. 3.7, the air domain radius influences the magnetic sensing results when it is below 0.25 m. The noise present in the results is due to the remeshing required when change the size of the air domain, but the overall change in magnetic flux density remains approximately 3.5% as long as the air domain radius is at least 0.3 m. Thus the air domain radius was set to 0.3 m to ensure the least required computational time while ensuring the effects of the boundary condition would not influence the magnet0-static results.

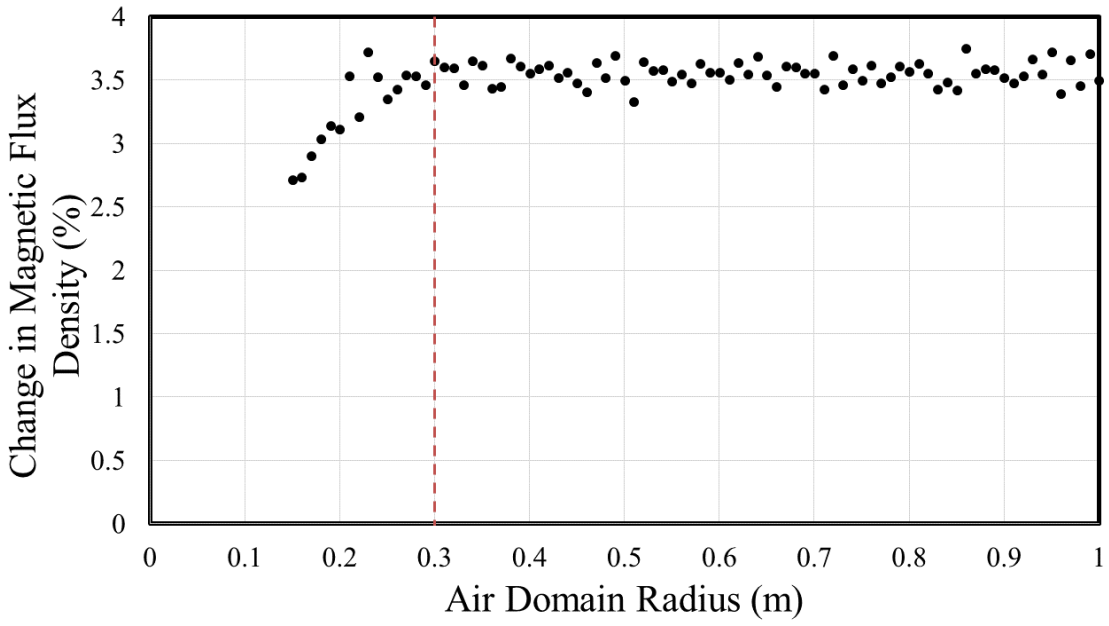

Figure 3.7: The air domain radius changes the results of the magneto-static model below a radius of 0.3 m.

3.3 Magnetization of FeMnAlNi

The magnetic properties of the MSMA wire are taken from magnetic testing calibration experimental data presented in Fig. 3.8. A FeMnAlNi sample is placed in a magnetic field with the magnetic long moment measured as a function of the magnetic field strength. It can be observed from Fig. 3.8 that the relation between magnetic flux density and magnetic field strength is linear below a saturation flux density value of 0.5 T; this linear relationship between magnetic flux density and applied magnetic field strength is defined by a material magnetic permeability. Beyond this region of linear magnetic permeability FeMnAlNi is in a saturated state of magnetization.

3.4 Validation of Magneto-Static Model

The magneto-static model is developed to facilitate the scripted and thus structured consideration of a range of geometric parameters using MATLAB [72]. This allows for the modification of parameters for validation against known experimental and analytical solutions, the generation of

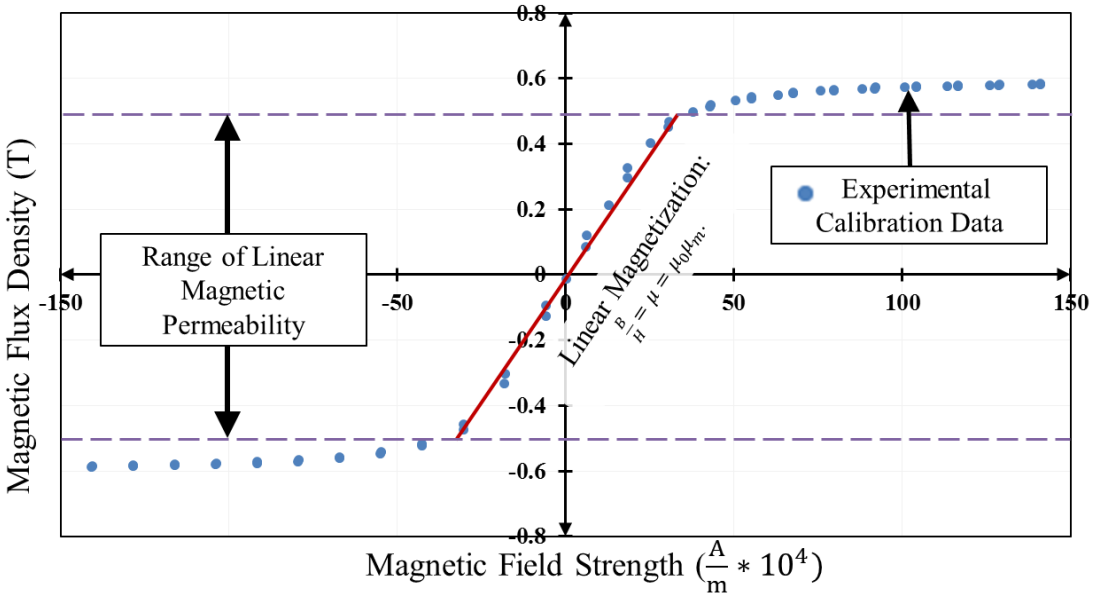

Figure 3.8: The magneto-static model relies on a linear relation between magnetic flux density and magnetic field strength in Austenitic FeMnAlNi.

various geometric configurations, and consideration of various locations of a permanent magnet or transformed MSMA region. The normal magnetic flux density is computed for a permanent magnet with the size and residual flux density B_r previously described considering a probe moving away from the magnet along its polar axis. These magneto-static results are then compared to the experimental results for the same geometric and magnetic parameters and to the known analytical solution for this simple geometry to validate the magneto-static model. The results are shown in Fig. 3.9, where the analytical solution is given as [73]:

$$B = \frac{B_r}{2}\left(\frac{L+z}{\sqrt{R^2+(L+z)^2}} - \frac{z}{\sqrt{R^2+z^2}}\right) \tag{3.1}$$

where B_r, L, R, and z are permanent flux density, permanent magnet length, permanent magnet radius, and distance from the permanent magnet face to the sensor along the polar axis, respectively.

Comparing (Fig. 3.8 and Fig. 3.9), it is observed that to satisfy the assumption of linear

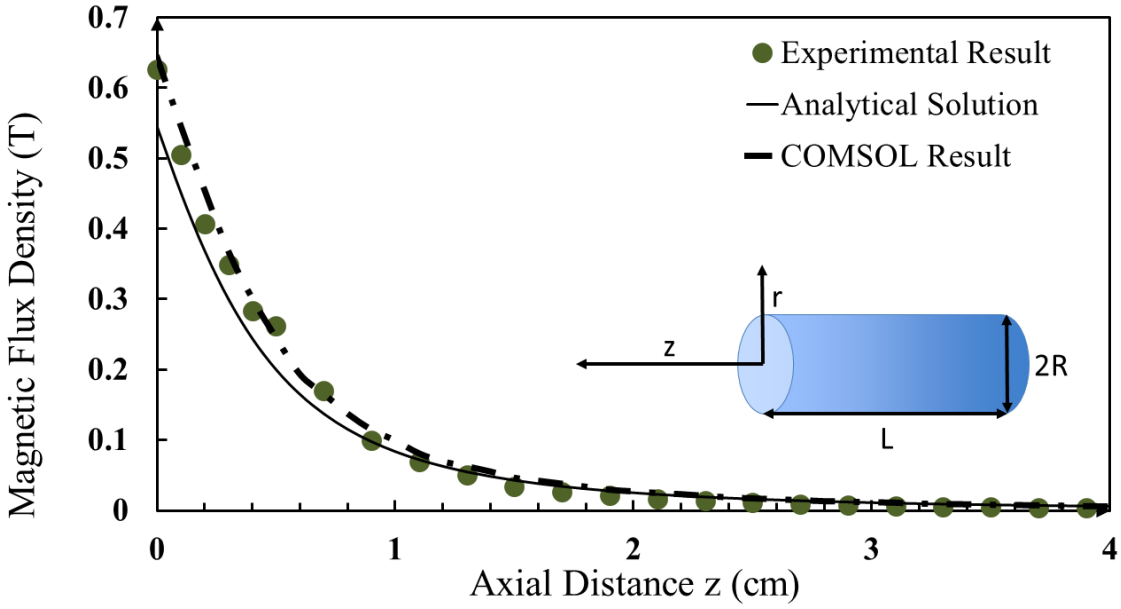

Figure 3.9: A comparison between computational results obtained from the magneto-static model, experimental results, and analytical solution for a simple geometry.

magnetization used in the modeling herein, the maximum magnetic flux in the wire must remain below 0.5 T, under which the linear relationship holds. The magnetic flux density along the magnet polar axis (Fig. 3.9) exceeds 0.5 T at 3 mm. Therefore, the distance from the MSMA wire to the face of the magnet will be greater than 3 mm for all cases considered herein, which is compatible with the target applications where MSMA reinforcements should not be located too close to the surface of structure.

3.5 Magnetic Flux Density Fields

A number of sensor locations were considered to determine the effect of sensor placement on the potential ability to measure the magnetic field. A complete profile of the changes in normal magnetic flux density mapped to the surface of a structure due to an embedded MSMA wire experiencing localized transformation is useful for understanding single sensor installation options or even the installation of multiple sensors for increased resolution. Thus, it is advantageous to visualize the change in magnetic flux density along the entire surface of the structure. First, the

change in the normal component of the magnetic flux density on an external face of the concrete block domain is calculated by comparing the normal magnetic flux density distribution when the wire is pure austenite to the altered normal magnetic flux density distribution after the development of a local, internal region of SIM in the MSMA wire, as shown in Fig. 3.10.

The altered magnetic flux density, shown in Fig. 3.10, differs depending on the relative location of the SIM region with respect to the permanent magnet. In the positions shown in Fig. 9, the change in normal magnetic flux density near the SIM region is higher on the same side of structure as the magnet (Fig. 3.10(a)). With a distance between the magnet and SIM region of 20 mm, the change in normal magnetic flux density peaks at over 0.1 mT on the surface coincident the magnet face and at 0.025 mT on the surface opposite the magnet. The change also increases as the distance between the SIM region and the magnet decreases. Thus, it is likely the local changes in normal magnetic flux density will increase as the location of the magnet relative to the SIM region decreases. Based on these computational results in normal magnetic flux density, the same side sensing configuration provides a higher sensitivity while also being a more practical method of implementation; whereby a permanent magnet and sensor might be integrated into a single scanning unit (e.g. a piece of hardware).

3.6 Modeling of Magnetic Sensing Methods

Having explored the magnetic fields near an MSMA wire with a local region of SIM, a method of external sensing is needed for practical application. External sensing configurations must be defined and simulated to demonstrate the measurable changes in the magnetic fields previously described.

3.6.1 Proposed Magnetic Sensing Configurations

External magnetic sensing requires a comparison of the measured magnetic flux density between the damaged and undamaged regions in a structure. In the current study, the location of the permanent magnet and the point of magnetic flux density evaluation are varied across the structure to determine the change in measured magnetic flux density due to a local region of internal

(a)

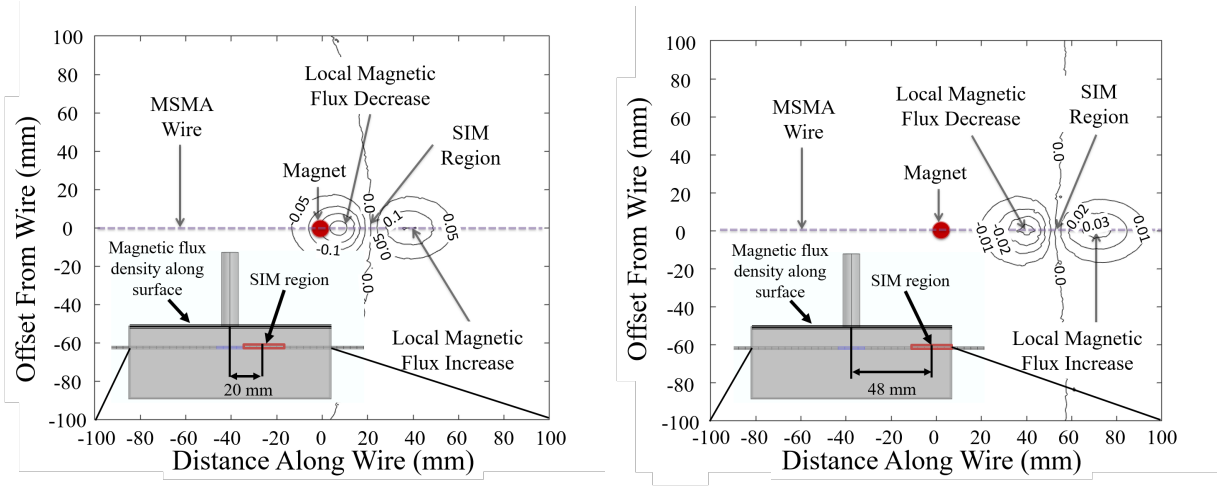

(b)

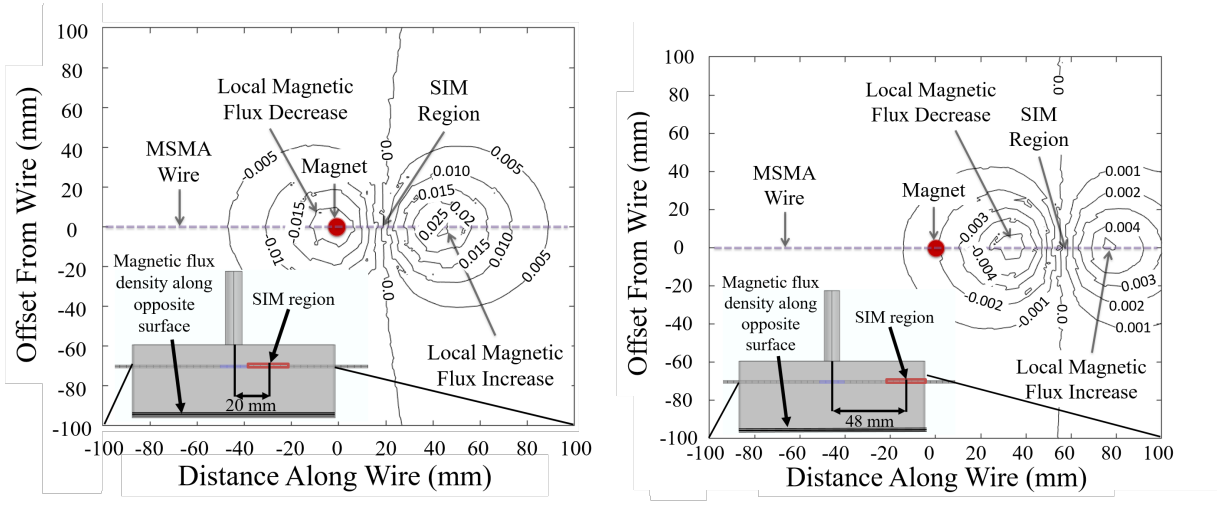

Figure 3.10: The change in normal magnetic flux density [mT] is evaluated on both the same surface as the magnet (a) and the surface opposite the magnet (b) when the SIM region of the MSMA wire is located 20 mm (left) and 48 mm (right) from the magnet.

damage. This internal damage leads to a change in local martensite volume fraction, $\xi(\mathbf{X})$, and creates a local region of stress-induced martensite (SIM), which can be searched for externally. The search for internal SIM regions, and thus internal damage, is simulated by moving a perma-

nent magnet along the surface of the concrete block parallel to the MSMA wire. The distances between the magnet, sensor, and wire are held constant; the only changes in computed magnetic flux density are due to local phase transformations in the MSMA wire.

Fig. 3.11 demonstrates the proposed coupled sensor and magnet configurations implemented into the magneto-static model. The relative location of the magnet and the point at which the normal magnetic flux density is measured (in the simulation of a Hall Effect probe) are held fixed and thus define a reference frame. We then wish to simulate the translation of this magnet/sensor pair along the axis of the wire in 4 mm increments. This is accomplished by partitioning the wire into 4 mm segments and applying the corresponding transformed and untransformed material properties to these wire segments as appropriate, updating them such that the intended relative motion between the wire and sensor is simulated.

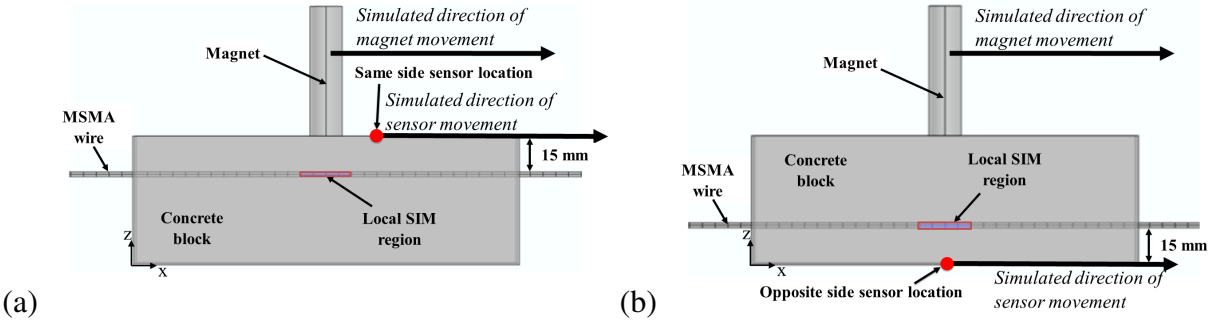

Figure 3.11: The proposed evaluation of internal damage requires an external magnet placed on the face of a structure, and the normal magnetic flux density measured at an external point. Opposite side sensing (a) assumes the sensor and magnet are on opposite sides of the block, while same side sensing (b) assumes the sensor and magnet are on the same side of the block.

As seen in Fig. 3.11, the magnet is located on the surface of the concrete block domain, with its polar axis perpendicular to that of the embedded MSMA wire. The position of the magnet along the x axis is measured relative to the center of the phase transformed region, which corresponds to the location of the internal crack. The geometry is configured in such a manner that

the proposed magneto-static model simulates the movement of an external magnet and sensor along the length of a structure either by placing the sensor on the opposite side of the structure (Fig. 3.11) or adjacent to the magnet (Fig. 3.11b), with the relative location of the sensor with respect to the permanent magnet location fixed. The benefits of each configuration will be addressed later.

3.6.2 Evaluation of Magnetic Sensing Configurations

Evaluating the change in magnetic flux density along the entire surface may require an array of sensors spaced close together to measure such changes, as these changes are shown to occur over local regions. For large structures, this may be a less practical means of implementation when compared to a single sensor moved across the structure. For opposite side sensing, the magnetic flux density is evaluated in more detail on the surface of the structure opposite the permanent magnet, aligned parallel with the MSMA wire at two locations: directly opposite the center of the magnet, and directly opposite its outer edge. These evaluation points are fixed with respect to the permanent magnet while the location of the local SIM region in the embedded MSMA wire is altered, thus simulating the scanning of the magnet/sensor pair past a damaged region.

Fig. 3.12 presents the normal magnetic flux density at a point located on the surface of the concrete domain opposite the permanent magnet, clarifying the effect of sensor placement relative to the magnet on the external magnetic sensing results as the wire is scanned. The magnetic flux density fluctuates by approximately 41 μT, or 1.1%, near the SIM region of the MSMA wire, as shown in Table 3.3. This is well above the demonstrated noise floor below 0.5 μT for a Hall effect probe [74] and above the 0.2% linearization error in many commercially available Hall probes [75], while other sensors such as Tunnel-Magneto-Resistance (TMR) sensor arrays may have sensitivities under 5 nT [76].

Two distinct exist for same side sensing. First, it facilitates evaluating a broad range of geometries via the use of a single hand-held device placed on the external surface of a structure.

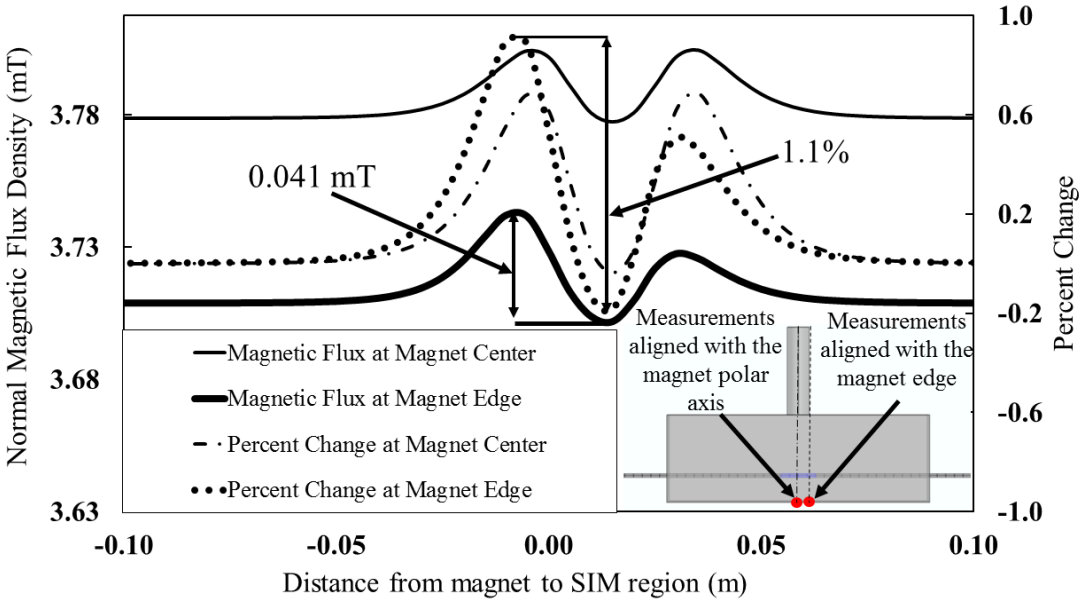

Figure 3.12: Opposite Side Sensing: The normal magnetic flux density at a fixed point fluctuates based on its location relative to an internal SIM region.

Table 3.3: Change in Magnetic Flux Density For Opposite Side Sensing Configuration

DISTANCE FROM MAGNET POLAR AXIS TO PROPOSED SENSOR [MM]	MAXIMUM CHANGE IN NORMAL MAGNETIC FLUX DENSITY [μT]	MAXIMUM CHANGE NORMAL MAGNETIC FLUX DENSITY [%]
0.0	27.1	0.72
6.35	40.6	1.10

This in contrast to the opposite side sensing (Fig. 3.12), wherein the magnet and sensor would require a carefully maintained alignment despite being on opposite sides of the structure. Secondly, it is associated with much stronger magnetic signals for a given amount of damage detected.

Fig. 3.13 shows the results for the magnetic flux density calculated at two separate distances from the polar axis of the magnet: 25 mm and 50 mm. Recall the cylindrical magnet has a

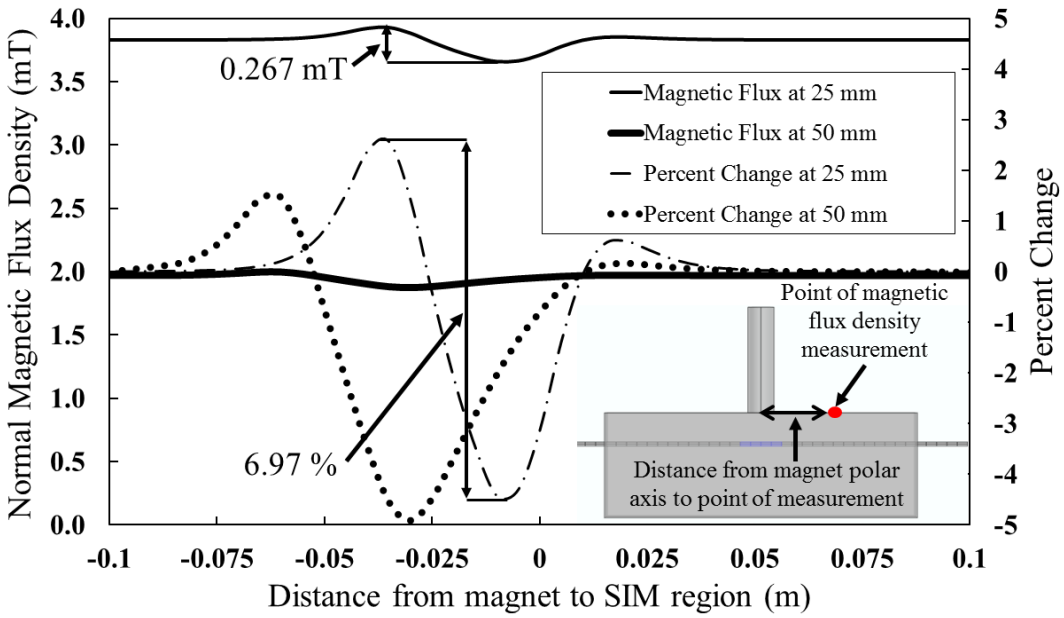

Figure 3.13: Same Side Sensing: The normal magnetic flux density near the SIM region when the magnet and sensor are on the side of the concrete block nearest the MSMA wire. The changes in magnetic flux density are larger than the opposite side sensing (Fig. 3.12).

radius of 6.35 mm. he magnetic flux density measured at 25 mm from the polar axis of the permanent magnet fluctuates near the SIM region of the MSMA wire by 267 μT, or 6.97% of the nominal normal magnetic flux density of 3.83 mT measured in regions far away from the SIM region of the MSMA wire. This is a significant improvement when compared to measurements made on the surface opposite the magnet (Fig. 3.12). When evaluating the magnetic flux density at 50 mm from the magnet polar axis, both the change in magnetic flux density and percent change in magnetic flux density decrease to 126 μT and 6.4%, respectively. These peak-to-peak fluctuations signify a measurable change in magnetic flux density near regions of SIM, which can be further improved upon by the addition of multiple sensors.

3.7 Effects of Embedded MSMA Wire Depth on Magnetic Sensing

Previous results (Figs 3.10, 3.12, 3.13) consider an MSMA wire embedded 15 mm away from the surface of the magnetic flux density evaluation. The embedded wire depth was then varied

Table 3.4: Change in Magnetic Flux Density For Same Side Sensing Configuration

DISTANCE FROM MAGNET POLAR AXIS TO PROPOSED SENSOR [MM]	MAXIMUM CHANGE IN NORMAL MAGNETIC FLUX DENSITY [μT]	MAXIMUM CHANGE IN NORMAL MAGNETIC FLUX DENSITY [%]
25	266.9	6.97
50	125.7	6.38

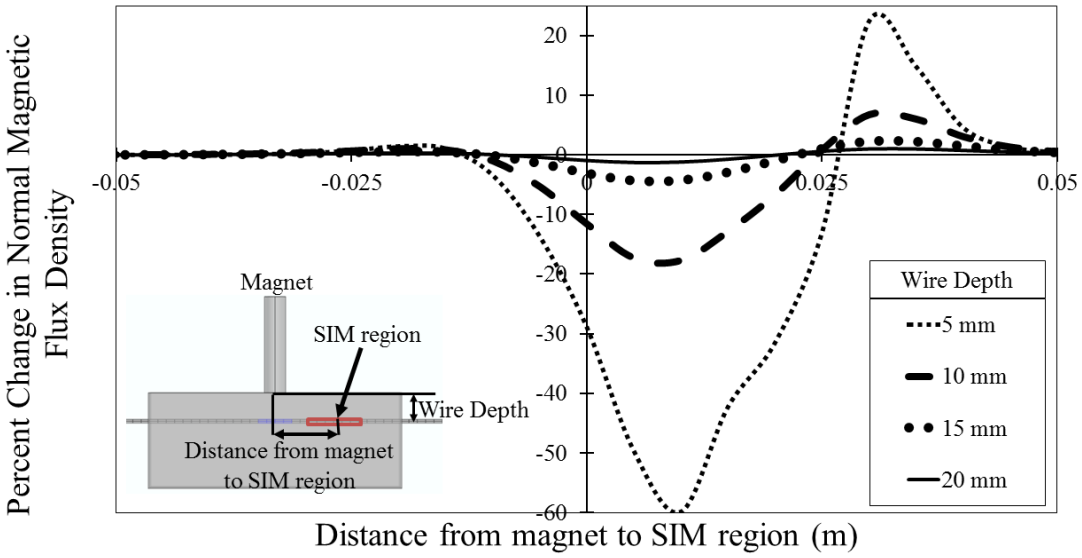

Figure 3.14: The normal magnetic flux density near the SIM region when the magnet and sensor are on the side of the concrete block nearest the MSMA wire.

from 5 to 20 mm to determine the trade-off between magnetic sensitivity and the embedded depth of the MSMA wire. This was performed under the same conditions as the same side sensing (Fig. 3.13) with 25 mm between the evaluation point to the magnet polar axis. As the MSMA wire is embedded deeper into the structure, the change in the normal magnetic flux density decreases sharply, as shown in Fig. 3.14. For a MSMA wire embedded at a depth of

Table 3.5: Change in Magnetic Flux Density at Different Wire Depths

WIRE DEPTH [MM]	MAXIMUM CHANGE IN NORMAL MAGNETIC FLUX DENSITY [mT]	MAXIMUM PERCENT CHANGE IN NORMAL MAGNETIC FLUX DENSITY
5	3.75	59.9
10	0.73	17.7
15	0.16	4.38
20	0.04	1.25

20 mm, the change in normal magnetic flux density drops to a 1.2% fluctuation of 43 μT, still well above the magnetic noise floor and standard sensor accuracies [74, 75, 76]. While increasing this distance will further decrease signal strength, it is important to note that all results consider an embedded wire of 1 mm radius. Increasing this diameter is expected to greatly increase signal strength. The changes and percent changes can also be seen in Table 3.5.

3.7.1 Conclusions of Embedded MSMA Wires in Concrete Structures

Embedded MSMA wires in concrete structures may be used to determine local internal damage via the change in magnetic properties which accompanies the transformation of austenite to stress-induced martensite (SIM) near stress concentrations and the local failure of concrete. The addition of SIM in an otherwise austenite MSMA wire will alter an externally applied magnetic field because martensite has a lower magnetic permeability than austenite. Near the SIM region of the MSMA wire, the lower local magnetic permeability in the region causes the magnetic flux density closer to the magnet to decrease while the local magnetic flux density outward of the SIM region will increase. The magnetic flux density in the presence of an externally applied magnetic is a function of the material properties of all the surrounding area, so a comparison of the magnetic flux near transformed and untransformed regions of the MSMA wire is necessary to determine if the region is damaged or undamaged via non-destructive evaluation (NDE). Two

means of NDE are proposed and evaluated, both consisting of a magnet and sensor moved along the outside of the structure. The location of the magnet and sensor are held constant with respect to each other and to the distance from the center of the MSMA wire. The normal magnetic flux density is measured as the magnet-sensor combination is moved parallel to the wire. Near regions of SIM, a fluctuation larger than the noise and errors of commercially available magnetic flux sensors [75] is observed in the measured external normal magnetic flux density, with a maximum peak-to-peak fluctuation of over 260 μT, or 6.7% for an MSMA wire embedded 15 mm in the concrete structure. However, a limitation for magnetic sensing may be how deep the MSMA wires are effective for NDE, as there is a significant decrease in magnetic sensitivity as the distance from the MSMA wire to the magnet-sensor combination increases. For wires located very close to structure surface, much larger changes in normal magnetic flux density are observed.

4. TRANSFORMATION OF LARGE GRAIN MSMA WIRES AND OTHER MSMA FORM FACTORS

4.1 Modeling of Large Grain MSMA Wires

4.1.1 Description of the Model

FeMnAlNi is a magnetic shape memory alloy which can be processed to have grain sizes of 4 mm [1]. In small MSMA wires such as those mentioned previously, this means these MSMA wires consist of single grains across the cross-section of the wire. Additionally, the transformation of such a wire from austenite to stress-induced martensite can be seen on a much larger scale than SMAs with much smaller grain sizes; a magneto-static model may be correlated to experimental work where the transformation of individual MSMA grains can be predicted. It is worth noting that large grain MSMA wires may be more susceptible to failure at the grain boundaries.

A magneto-static model was developed to correlate the change in an external magnetic field to the transformation of individual large grains of an MSMA wire under an applied magnetic field. The model consists of a permanent magnet, a small MSMA wire, and an active area of a sensor as shown in Fig. 4.1. The MSMA wire consists of grains larger than the cross-section of the MSMA wire. The grain boundaries are thus consistent across the cross-section of the wire.

The purpose of such a model is to validate the computational solution to the measured magnetic flux density from an experimental measurement. Thus, the model must consider different orders in which the transformation of grains may occur in an MSMA wire. Experimental work has been conducted by Karaman et al [1] to measure the change in a local magnetic field as a large grain MSMA wire is put under increasing cycles, inducing a transformation from austenite to martensite in the wire. A neodymium magnet with a remanent magnetic flux of 1.3 T was placed $\approx$1.5 mm from the MSMA wire to generate a static magnetic field. A Hall effect probe was employed to evaluate the local normal magnetic flux density $\approx$3 mm from the magnet face, with the MSMA wire between the magnet and probe. The measured normal magnetic flux den-

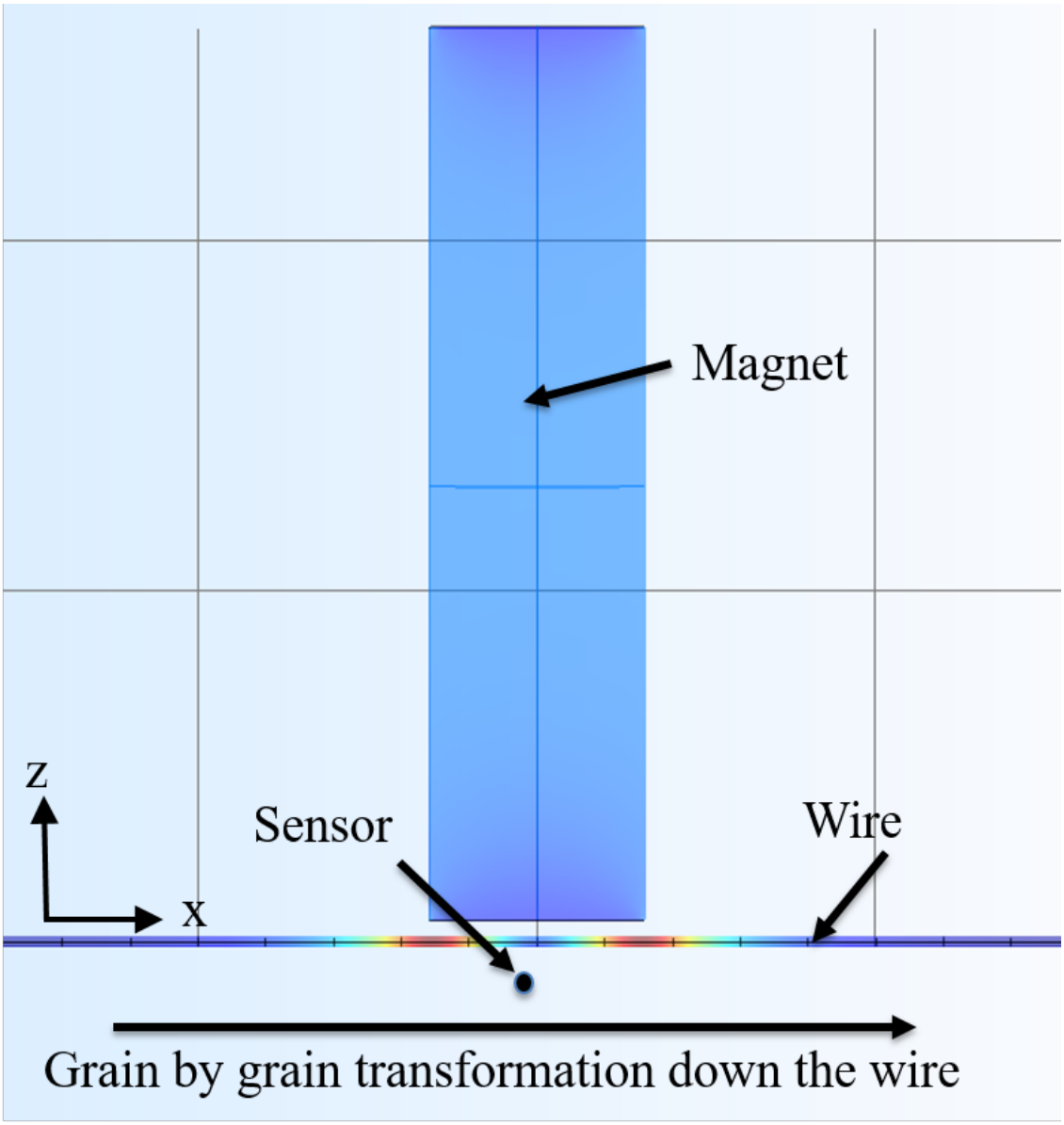

Figure 4.1: The magneto-static response of FeMnAlNi wires composed of large grains can be modeled by the transformation of individual grains from austenite to martensite.

sity was measured as the MSMA wire underwent loading cycles of increasing strains, from 0 to 8% in 1% increments. The wire transformed from austenite under no strain to martensite under higher strains, and then returned to austenite when unloaded. A local permanent magnet is placed near the MSMA wire, with a Hall probe positioned opposite the magnet as pictured in Fig. 4.1.

While evaluating the normal magnetic flux density at a discrete location is valuable, experimental results require an active sensing area. Close to a transforming MSMA wire with large grains as pictured in Fig. 4.1, the magnetic flux density gradients near individual grain boundaries can be much larger than those in air.

The effect of a finite sensing area (as compared to a discrete point evaluation) was implemented into the magneto-static model based on the active area of the Hall effect probe. The active area was taken from the specifications for a Lake Shore axial Hall probe [75], as used in the experiment described previously. For transformations between grains, the large gradients between austenite and martensite grains can be seen in Fig. 4.2. The magnetic flux density through the MSMA wire varies strongly based on the phase of the material.

4.1.2 Effect of Large Grain Boundaries on Magnetic Sensing

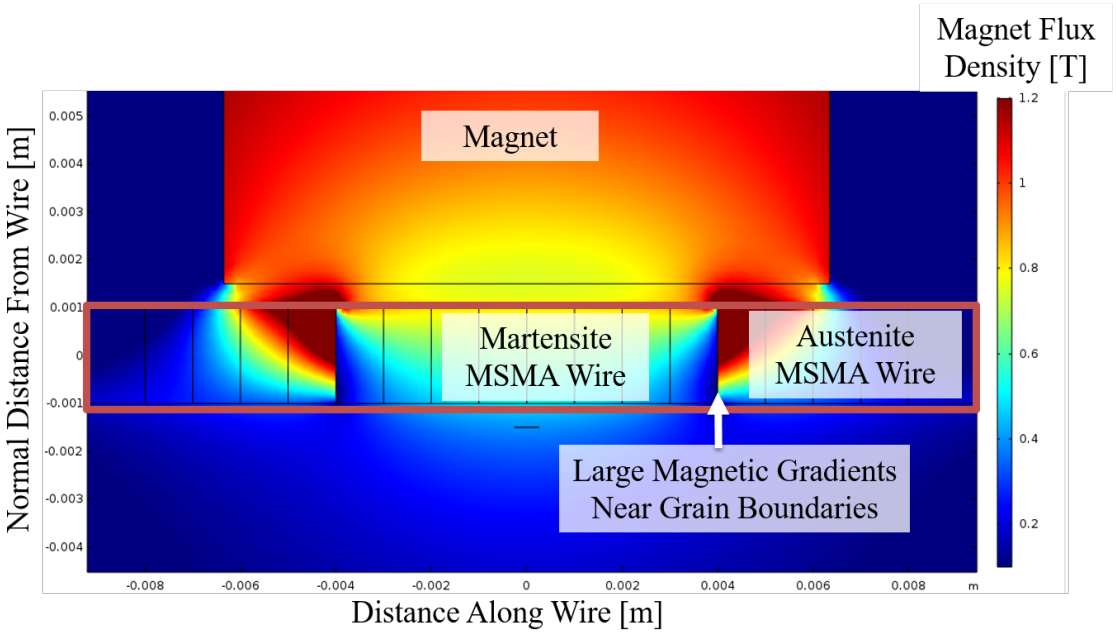

Figure 4.2: Large magnetic flux gradients occur between grain boundaries between austenite and martensite in the presence of an applied magnetic field.

It can be seen in Fig. 4.2 that large fluctuations in the magnetic field may occur near the grain boundaries of MSMA wires. While these grain boundaries are clearly defined in the magneto-static model, they may not be known of defined for embedded magnetic MSMA wires in infrastructure, or even in experimental data. Thus, the effect of individual grain boundaries between austenite and martensite in MSMA wires may cause large fluctuations in magnetic sensing results when the boundary occurs very close to the magnetic sensing method.

4.1.3 Response of a Finite Active Sensing Area

Baseline observations of the magnetic field near the MSMA wire were conducted without boundaries and varying phases of the wire. The magneto-static field boundary value problem was solved for wires of aluminum, austenite FeMnAlNi, and martensite FeMnAlNi. Aluminum serves as a baseline for the original magnetic field while maintaining the geometry of the model, as it is unmagnetizable. The normal magnetic flux density was then plotted into the magnet, wire, and Hall probe face to compare the effect of each wire on the magnetic field, as shown in Fig. 4.3.

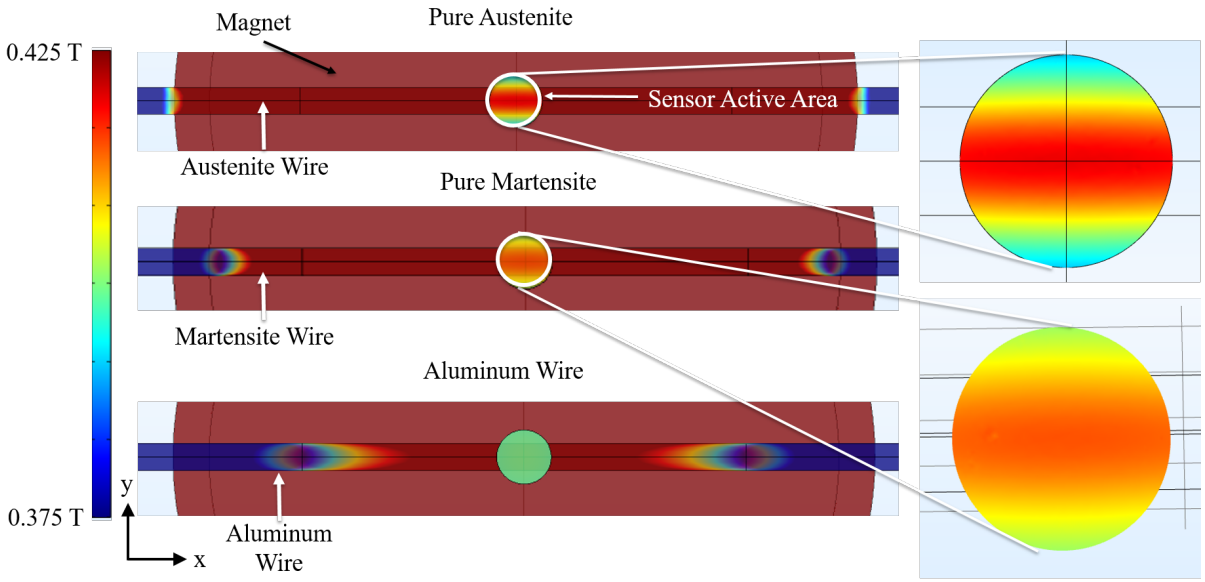

Figure 4.3: Gradients form on the sensor active area as the regions near it become more unevenly magnetized.

While the presence of aluminum has a minimal effect on the local magnetic properties of the region due to similar magnetic permeability to air, the increased magnetic permeability and polarization in both austenite and martensite leads to increased gradients and overall magnetic flux across the nearby sensor face. Regions of the sensor face aligned with the wire saw increased normal magnetic flux density near the MSMA wires compared to the sensor face near the aluminum wire.

With the sensor face, variable grain sizes, and different materials defined previously, the next step in the model is to determine the effects of the large grains, and their respective boundaries, on the readings of a Hall effect sensor active area. The model was defined as shown in Fig. 4.1 with a FeMnAlNi MSMA wire with 4 mm long grains. The normal magnetic flux density on the magnet face experiences a strong gradient due to the local phase transformation from austenite to martensite when the grain boundary between austenite and martensite is nearby, as can be seen in Fig 4.4. This could be used to determine the exact location of phase transformation in large grain MSMA wires.

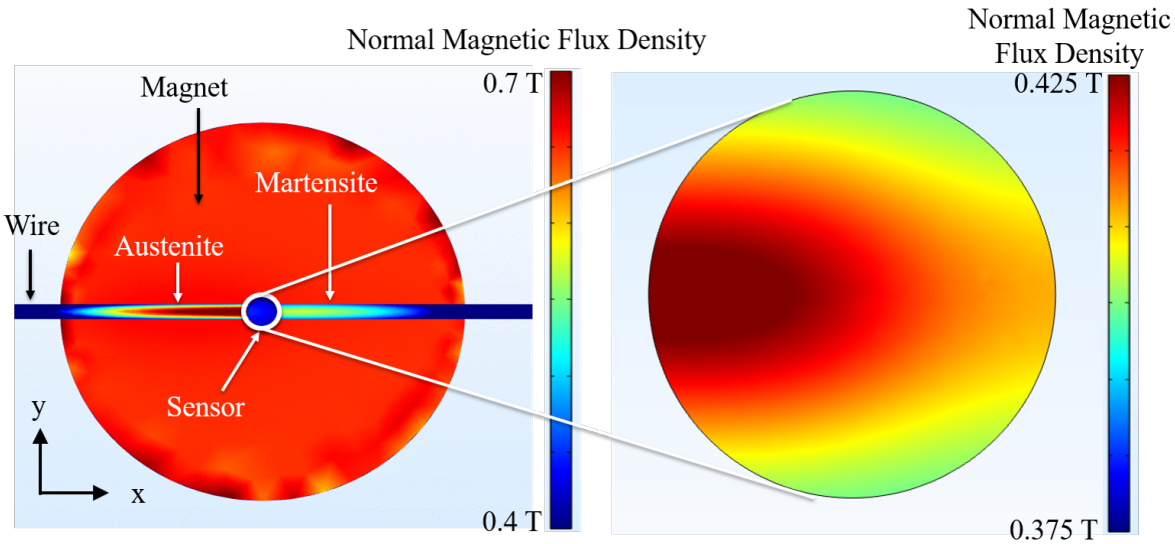

Figure 4.4: A grain boundary between the austenite and martensite phases of the FeMnAlNi wire leads to a large magnetic flux gradient on the active area of a nearby sensor.

4.1.4 Grain by Grain Transformation of an MSMA Wire

The transformation of the wire was then evaluated in the magneto-static domain for a single point, located at the center of the sensor location. The grain by grain transformation originates at one end of the wire, with each neighboring grain transforming sequentially. The measured normal magnetic flux density changes rapidly when the grain boundary is located near the sensor, as shown in Fig. 4.5.

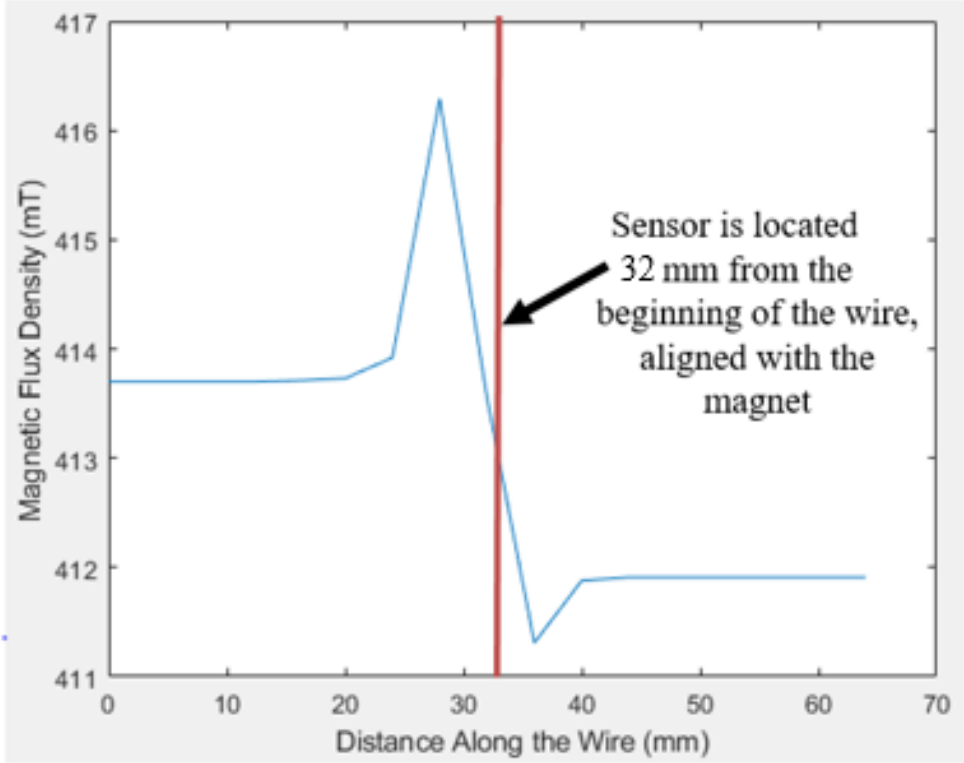

Figure 4.5: As the MSMA wire transforms from austenite to martensite, the measured normal magnetic flux density between the sensor and magnet undergoes a large fluctuation before decreasing.

The normal magnetic flux density measured by the magnet observes a large increase, then decrease near the boundary between austenite and martensite grains due to the large gradients

seen in Fig. 4.4. This indicates a large fluctuation in magnetic flux density such as the one seen Fig. 4.5 can be attributed to a boundary between austenite and martensite grains in a nearby embedded MSMA wire. However, the local normal magnetic flux density due to the presence of austenite and martensite has already been shown to both increase near the MSMA wire and decrease in the direction normal to the MSMA wire. Therefore a closer look at the effects of a transforming MSMA wire on a local magnetic sensor is needed to explain the various effects of the MSMA grain transformation on any means of measurement.

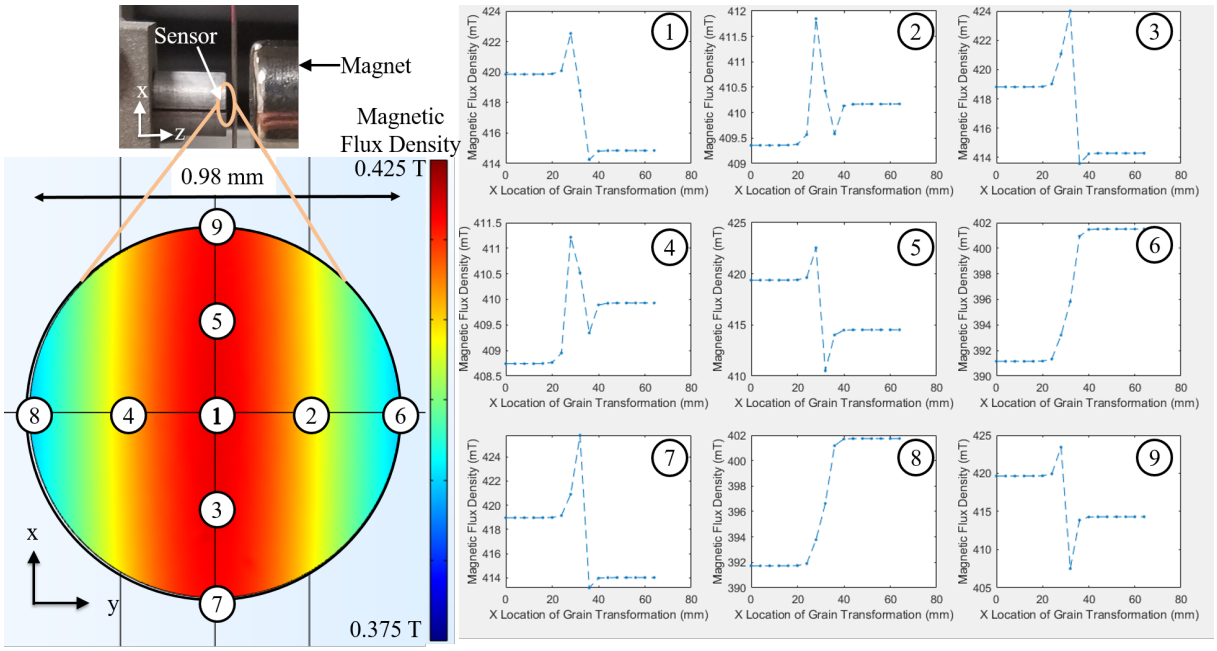

Figure 4.6: A magnetic sensor experiences vastly different responses over its active area in the presence of austenite-martensite grain boundaries.

Various locations aligned with the x and y axis on the sensor face were chosen to determine the change in magnetic field as the MSMA wire transforms from austenite to martensite. The configuration of magnet, sensor, and measured locations can be seen in Fig. 4.6. The single point evaluation at the center of the sensor (pt. 1 in Fig. 4.6) shows the same trends as the overall

sensor. There is a large fluctuation near the austenite-martensite grain boundary and a decrease in the measured normal magnetic flux density as the wire transforms from austenite to martensite. However, the trends at points 6 and 8 show the opposite trend, in that the magnetic flux density actually decreases as the wire transforms from austenite to martensite. Additionally, the overall change over the face of the magnet decreases by 1-2%, a similar trend to experimental results from cycling large grain MSMA wires [1].

4.1.5 Overview of Large Grain MSMA Transformation

Noting that the addition of wires and cables increase the strength of concrete as structural reinforcements [17, 18], MSMA wires with large grain sizes have been modeled as partitioned individual grains, each with austenite or martensite material properties. A sensor can be modeled either as an independent domain or a series of points to simulate a real world application or magnetic sensing using a Hall effect probe. As the grains in the wire transform, grain boundaries between austenite and martensite grains lead to large fluctuations in the magnetic field. These fluctuations can be detected by measuring the normal magnetic flux density on the side of the structure. Thus, in the case of local stress concentrations leading to the creation of stress-induced martensite grains, the grains can be detected either by the overall change in normal magnetic flux density or the large fluctuations caused by boundaries between austenite and martensite grains.

4.2 Modeling of Embedded MSMA Cables

Based on the previous transformation of a MSMA single wire, the effect of transformed segments of braided cables on measured magnetic flux is investigated. The braided cable magnetostatic model consists of a series of 6 wires wrapped around a straight wire located along the polar axis of this cable, a configuration referred to as a 1x7 cable, or wire rope. The cable is defined parametrically in COMSOL by the number of wires in the cable, the cable twist, and size of the individual wires. Each individual wire has a radius of 1 mm, with an axial pitch of 50 mm/rotation defined by a Bezier curve. Each wire is then grouped into a single cable material domain. Material properties of the braided cable are assigned to individual segments based on

partitions along the length of the cable material domain. The model is shown in 4.7.

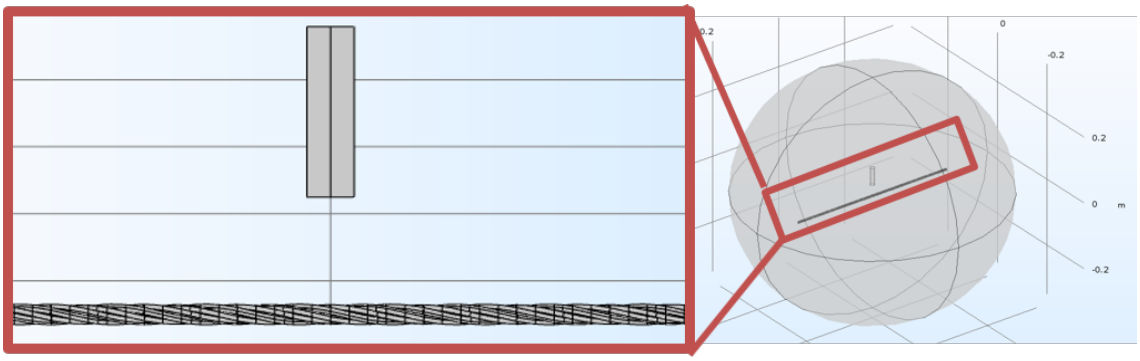

Figure 4.7: The magneto-static model for the braided cable consists of a permanent magnet and a 7x1 braided cable encompassed by an air domain.

The relative magnetic permeability of air and concrete are both incredibly close to 1.0, and as such can incorporated into the singular air material domain. This simplifies the required meshing between material domains by removing boundaries between domains with the same material magnetic properties, and thus the magneto-static model will henceforth refer only to the air, magnet, and cable domains. The cable is meshed using 3D tetrahedral elements, as shown in Fig. 4.8.

The cable is composed of FeMnAlNi, and the untransformed cable is in pure austenite with a relative magnetic permeability of 16, or a magnetic permeability of 2.01e-5 [H/m]. This initial configuration is solved to serve as a baseline to compare the effect of SIM in the cable on the overall magnetic field, as the existence of the cable with affect the magnetic field. The magnetic flux density for this austenite MSMA wire is shown in Fig. 4.9. The higher magnetic permeability in the austenite FeMnAlNi increases the magnetic flux density along the polar axis of the cable domain.

Next, regions of SIM are introduced into the MSMA cable, as would occur from the stress concentration and loading from internal damage. In this study, a local region of the cable domain is transformed into SIM to evaluate the change in the magnetic field between the original, fully

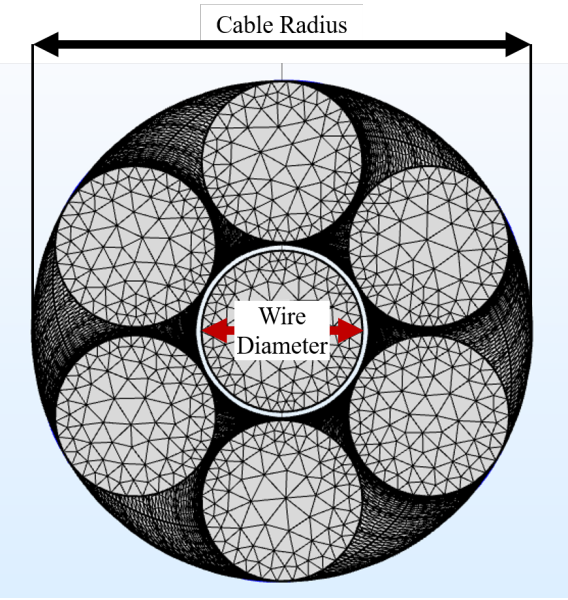

Figure 4.8: The braided cable magneto-static model consists of 6 MSMA wires wrapped around a center wire, meshed with tetrahedral elements.

austenite cable and the same cable with a local region of SIM. The magneto-static boundary value problem is solved for both the fully austenite MSMA cable and then for the austenite cable with a local region of martensite. The normal magnetic flux density is then evaluated along the XY plane for two values of Z: tangent the face of the magnet and 50 mm away from the face of the magnet.

For a large number of normal magnetic flux density evaluations, the symmetry of the magnetic field, as seen in Fig. 4.10, the local magnetic flux density will be symmetric on the YZ plane. Fig. 4.10 shows the magnetic flux density through the XY plane 50 mm from the face of the magnet. Due to the cylindrical geometry of the magnet, the field does not quite exhibit polar symmetry (it has been established that the presence of an MSMA wire will alter the field) but will exhibit symmetry across the XZ plane. Thus, a change in the normal magnetic flux density between two points the same distance away from the magnet in the x direction signifies a change in the material properties in the magnetic field. These planes of evaluation are the same as those used to determine the change in magnetic flux density along the surface of the concrete block-

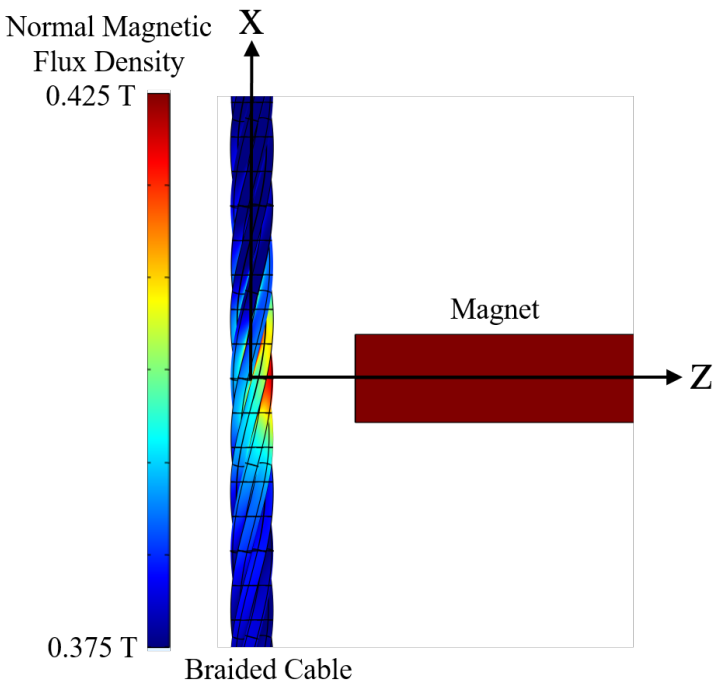

Figure 4.9: The normal magnetic flux density through a magnetizable cable before transformation.

MSMA composite previously discussed. This allows for a comparison of the change in normal magnetic flux density in both single wires and cables for a given phase transformation in the MSMA components.

The change in normal magnetic flux density on both sides of the MSMA cable can be seen in Fig. 4.11. The plane tangent to the face of the magnet shows a larger change in magnetic flux density than the single wire evaluated at the same locations. The magnetic flux density evaluated tangent to the face of the magnet exceeds 600 μT for the braided cable, while for a single wire the maximum change in magnetic flux density was under 200 μT. To simulate this measurement with respect to the axial location of the SIM region, the location of the magnet in the x direction is varied incrementally with respect to MSMA cable-concrete block composite. The normal magnetic flux density is measured 50 mm away from the face of the magnet, along the magnet polar axis.

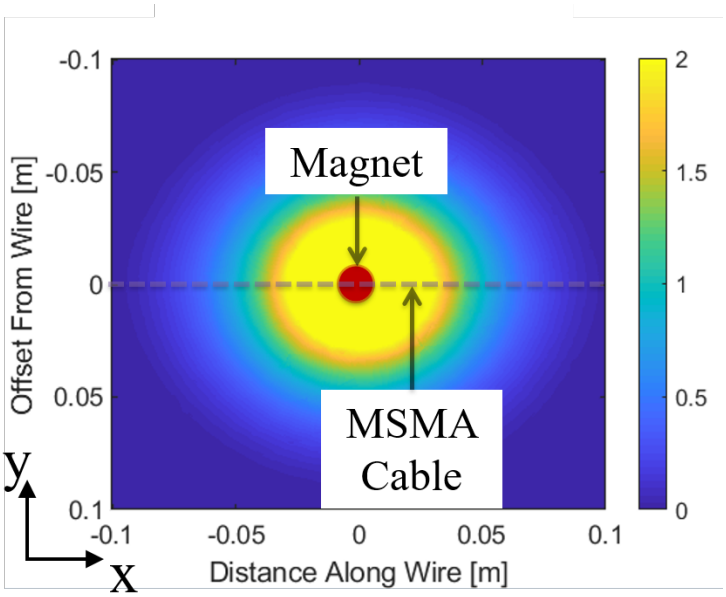

Figure 4.10: The normal magnetic flux density through the XY plane 50 mm from the face of the permanent magnet. For an untransformed MSMA cable, the magnetic field is symmetric along the YZ plane.

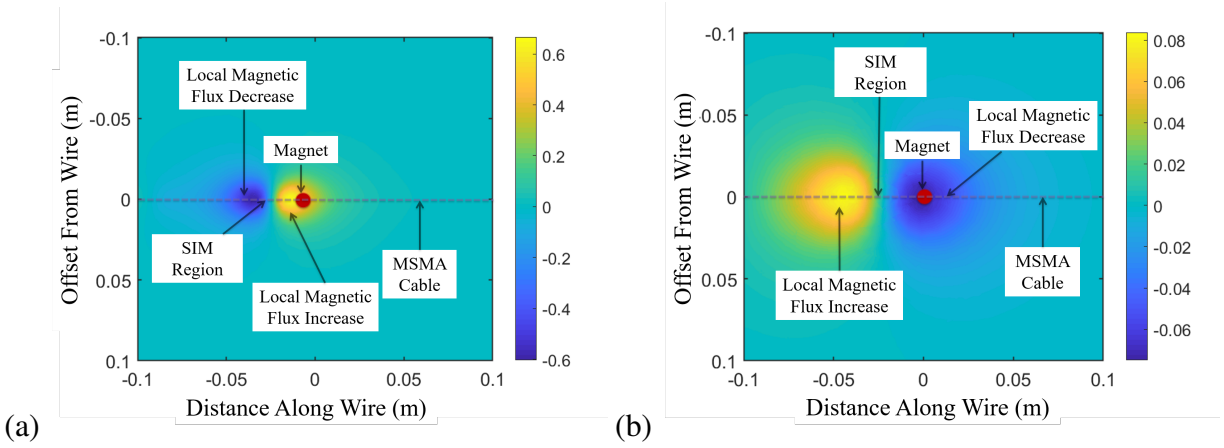

Figure 4.11: The change in normal magnetic flux density [mT] increases near local regions of transformed MSMA cables from (a) a plane tangent to the magnet face and (b) a plane 50 mm away from the magnet face.

4.2.1 Overview of the Magneto-Static Response of Embedded Braided MSMA Cables

Overall, the braided cable shows a similar magnetic response to the single wire, but a change in the magnetic properties across the braided cable results in a larger change in the externally applied magnetic field due to the increase in mass. This may prove useful for embedding MSMA cables deeper into structures, as increasing the cable or wire depth decreases the magnetic response. The results showed that the smaller the distance between the magnetic flux density measurement and the wire, the larger the change in magnetic flux density. There was a maximum change in normal magnetic flux density of over 600 μT due to the phase transformation of a local region in the MSMA cable.

5. EMBEDDED MAGNETIC SHAPE MEMORY ALLOY PARTICLES

The use of embedded SMA wires in a concrete matrix was chosen due to the multi-functionality of SMAs in civil infrastructure. In aerospace structures, metals such as aluminum are much more commonly used than concrete due to higher ductility, better tensile properties, and higher strength to weight ratios. While embedding SMA wires presents manufacturing challenges in aluminum not present in concrete, previous work has embedded MSMA particles in an aluminum matrix. This work demonstrated that NiCoMnSn could be embedded into an aluminum host, transform under damage from an internal crack, and maintain its original material strain-based magnetic response after processing [77]. A computational model is developed to compute the magneto-static response of such an aluminum-MSMA composite based on transformation of the embedded MSMA particles.

5.1 Modeling of a Single Embedded MSMA Particle

5.1.1 Description of the Model

A single-particle magneto-static FEA model, shown in Fig. 5.1, consists of a spherical MSMA particle embedded in an aluminum sheet, with a permanent magnet on one side of the concrete block generating a magnetic field. The performance of the permanent magnet is defined by its residual flux density of B_r = 1.3 T, a common residual flux density for commercial AlNiCo and Neodymium N42 magnets [71]. The effects of embedded MSMA particles on an applied magnetic field were investigated for a single MSMA particle embedded in an aluminum host. Aluminum has a material magnetic permeability almost identical to free space, and an aluminum sheet was modeled as a flat plate with a thickness of 5 mm. The dimensions of the single particle magneto-static model are shown in Table 5.1.

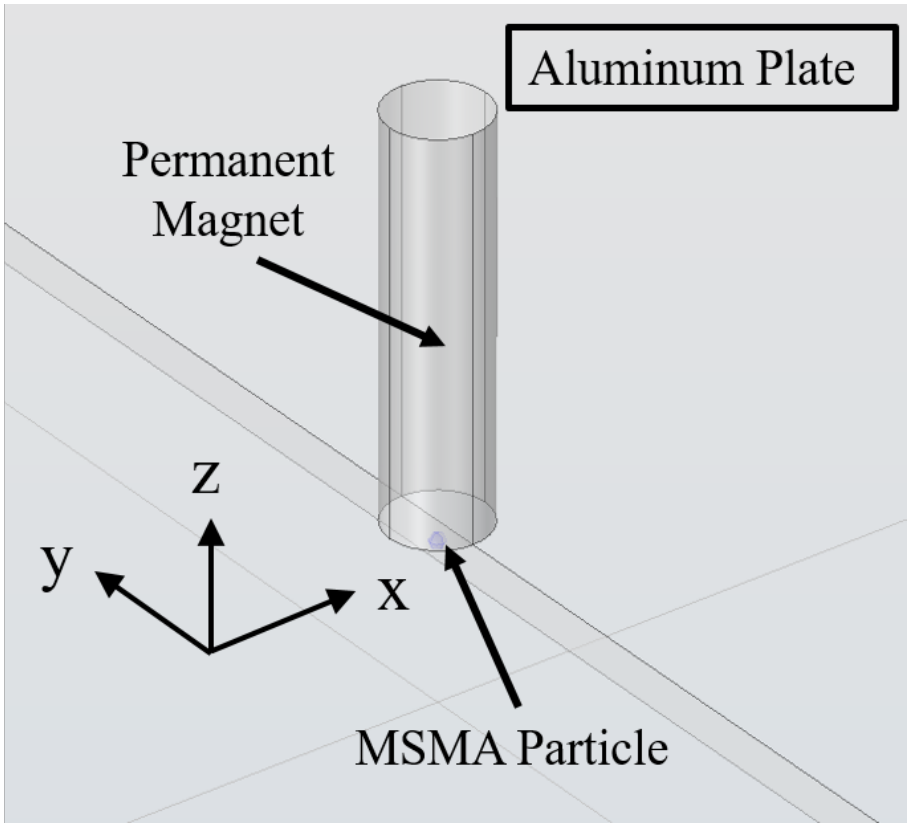

Figure 5.1: The magneto-static model consists of a segmented MSMA wire embedded in a concrete block with a magnet placed on one side of the block.

Table 5.1: Single Particle Magneto-Static Model Parameters

PROPERTY	VALUE	DESCRIPTION
t_{Plate}	5 mm	Aluminum Plate Thickness
L_{Plate}	500 mm	Aluminum Plate Length
$R_{Particle}$	0.5 mm	MSMA Particle Radius
L_M	50.8 mm	Magnet Length
R_M	6.35 mm	Magnet Radius
B_r	1.3 T	Magnet Remanent Flux Density

5.1.2 Magnetic Trends of Embedded MSMA Particles

The magnetic permeability of the MSMA particle was altered and the change in magnetic field computed. The particle relative magnetic permeability was decreased from a magnetizable material with a relative permeability of 16 to an unmagnetizable material with a relative magnetic permeability of 1. The normal magnetic flux density for a point on the opposite side of the aluminum surface aligned with the magnet polar axis can be seen in Fig. 5.2.

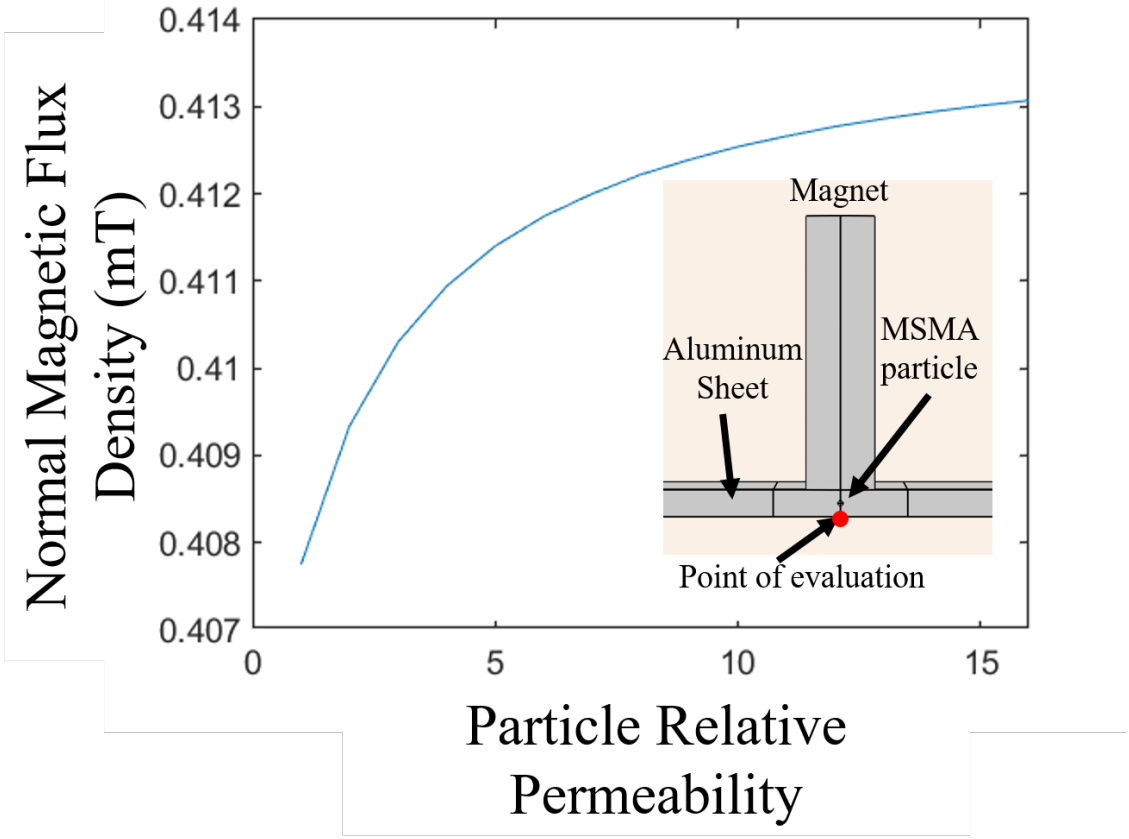

Figure 5.2: The normal magnetic flux density opposite the magnet increases as the relative magnetic permeability of the embedded particle increases.

As a single embedded particle in an aluminum transforms from a magnetizable to unmagne-

tizable domain, the magnetic field is altered around the local change. The change in the magnetic field, due to the change in polarization of the MSMA particle, is based on both the properties of the MSMA-aluminum composite and the parameters of any magnetic sensing devices, such as the permanent magnet. An initial investigation into the effect of the magnet shape and MSMA particle size is conducted to determine if any geometric effects can be isolated and set as constant values. The study solves for the MSMA particle with a magnetic permeability of 16, such as that of FeMnAlNi to solve the magnetic field equations for a magnetizable particle in the austenitic phase. The magnetic field is then solved for a unmagnetizable MSMA particle in the martensite phase. An evaluation point was then chosen as the point along the polar axis of the permanent magnet on the opposite side of the aluminum sheet. The normal magnetic flux density was then evaluated for when the MSMA particle was in the austenite and martensite phases. A full factorial design of experiment (DOE) was then performed to evaluate the effect of particle radius, magnet radius, and magnet length on the change in normal magnetic flux density at the specified evaluation point. As typical magnetic sensors have both a linearity error and a minimum noise threshold, both the change and percent change in normal magnetic flux density were evaluated, as can be seen in Fig. 5.3.

5.1.3 Conclusions of Embedded Single Particle MSMAs

The DOE results from Fig. 5.3 show the largest effect on the change in magnetic flux density is due to the size of the MSMA particle. As the amount of MSMA added into the aluminum sheet may become cost prohibitive and increase the surface area of boundaries between the MSMA and aluminum matrix, this may lead to a trade off between embedded MSMA material used and magnetic sensing range. The effects of magnet radius and length are less significant, but a longer permanent magnet appears to increase the change in magnetic flux when compared to the initial normal magnetic flux density. Perhaps most importantly, the ranges of change in normal magnetic flux density are well above established sensing thresholds for Hall probes and Tunnel Magneto-Resistance (TMR) sensors [74, 75, 76].

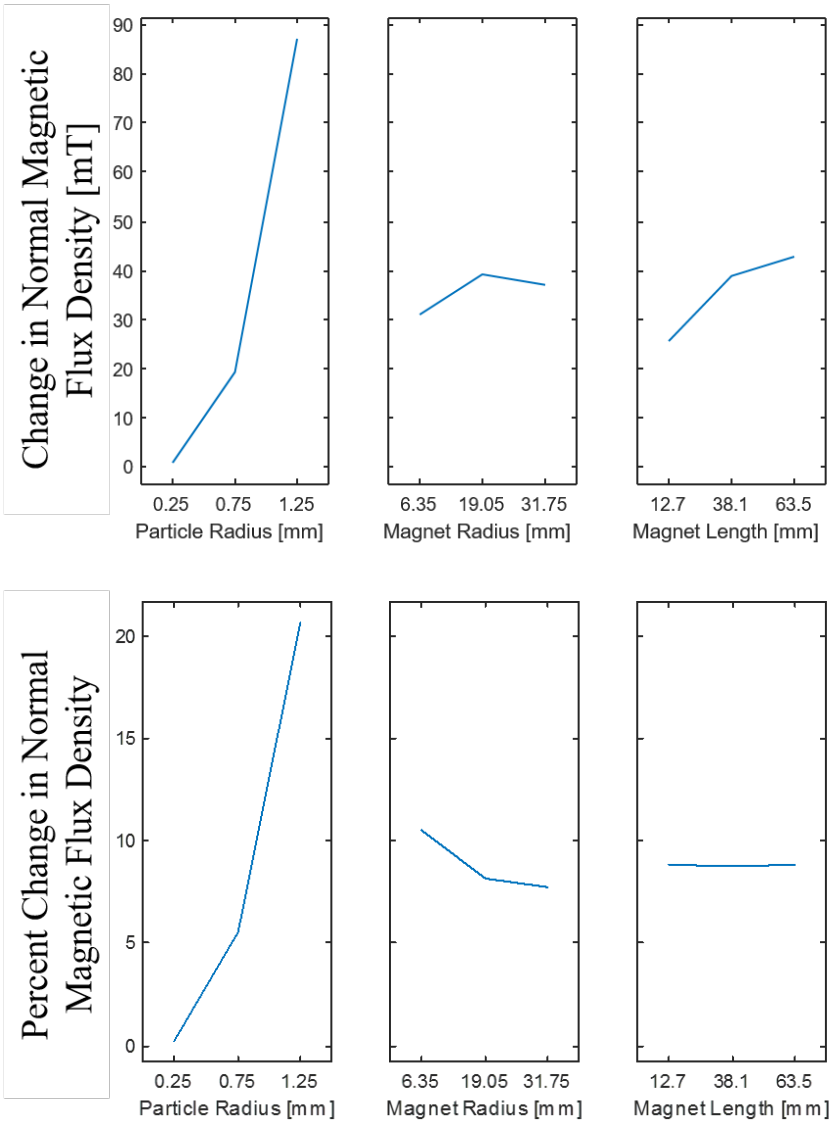

Figure 5.3: DOE results for the change in normal magnetic flux density due to an embedded MSMA particle transforming from magnetizable austenite to unmagnetizable martensite.

Since the geometric parameter with the largest effect on the measurable change in an external magnetic field was clearly the size of the MSMA particle, increasing sensitivity requires replacing more of the aluminum sheet with MSMA material. Beyond the previously cited works by Nicholas Barta [77] and Brent Bielefeldt [52], the effects of larger MSMA particles on the structural integrity of the material is lacking, and would need to be investigated further. The effects

of interactions between different particles in the magneto-static domain is also not considered for the single particle, while local transformation would required nearby particles, and thus numerous particles in a single region, as done in the work by Bielefeldt. This either requires a large number of very small and randomly dispersed particles in a much large aluminum matrix, which is very computationally intensive and inefficient, or a composite model of a homogeneous mixture of embedded particles in an aluminum host.

Additionally, while these initial studies were to identify the trends in magneto-static modeling of embedded MSMA particles, the particles developed in the work done by Barta had a radius of approximately 0.03 mm. For even a 2% volume fraction in a 5 mm cube, which would account for the full aluminum thickness used in the model, over 20,000 particles would be needed. Thus a homogeneous approach was needed, which will now be discussed.

5.2 Composite Modeling of Embedded MSMA Particles

The previous section details the transformation of a single large, isotropic MSMA particle near an applied magnetic field. A technique for embedding MSMA particles in an aluminum host which has been performed and tested to ensure similar material strength involves much small particles dispersed in a less-predictable manner. For a single particle, the location of the particle with respect to the permanent magnet will change the magnetic field. This requires knowledge of the exact location of every particle, which may not be feasible in a large structure such as an airplane. An aluminum matrix with large number of small MSMA inclusions would allow for a composite with homogeneous magnetic properties. Knowledge of the individual MSMA particle locations and relative sizes can be simplified to a homogeneous mixture based on the volume fraction of MSMA particles using effective medium approximations (EMA) for the magnetic properties.

5.2.1 Description of the Composite Model

EMA allows for the calculation of homogeneous material properties as an alternative to randomly dispersing small MSMA particles, and the subsequent mesh refinements required to per-

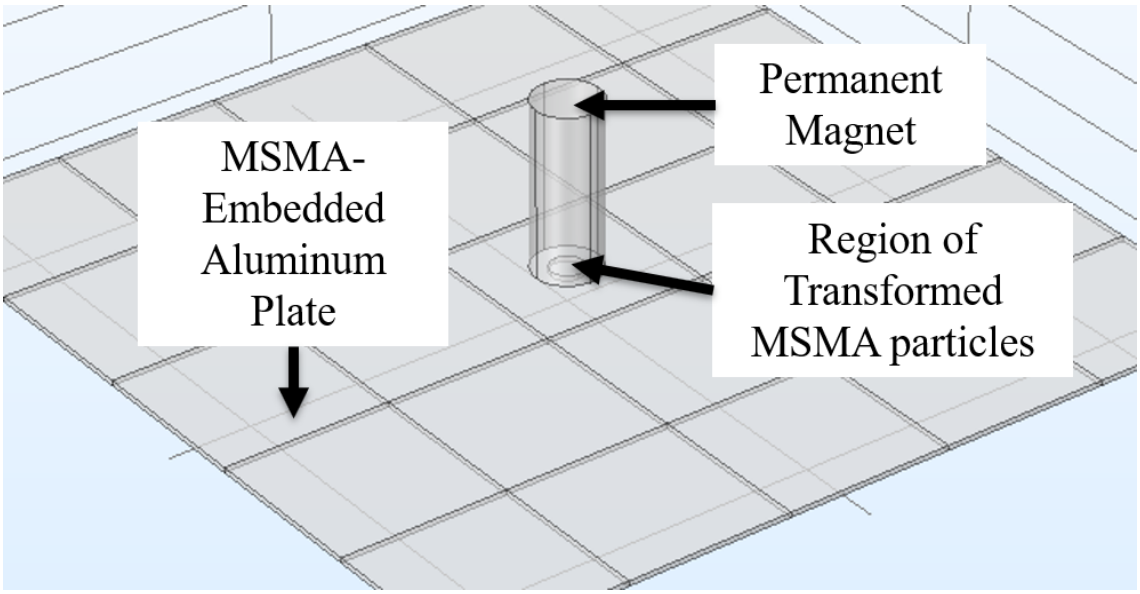

Figure 5.4: In this composite model, regions of the MSMA-aluminum composite are defined by the homogeneous magnetic properties of the region as opposed to individual aluminum and MSMA material domains.

form finite element analysis (FEA) on particles order of magnitude smaller than the aluminum host region. Thus, local regions can be defined by the state of the embedded MSMA particles in each region based on their martensite volume fraction ξ, as seen in Fig. 5.4.

A reference model is defined as a homogeneous aluminum-MSMA composite in which the MSMA particles are in the austenite form, untransformed by damage. A permanent magnet is placed in the center of the aluminum-MSMA composite generating a magnetic field magnetized due to the presence of magnetizable MSMA austenite. All changes in measured magnetic flux density are compared to this reference configuration to determine the measurable change in magnetic flux density due to local transformation in the MSMA particles.

5.2.2 Determining the Magneto-Static Effects of Embedded MSMA Particles in an Aluminum Host

First, the magneto-static model in Fig. 5.4 is solved over a range of MSMA particle volume fractions in which the MSMA particles are magnetizable as austenite. The normal magnetic flux

density is evaluated on the face of the composite opposite the magnet, aligned with the polar axis of the magnet. The change in normal magnetic flux density for different MSMA volume fractions can be seen in Fig. 5.5.

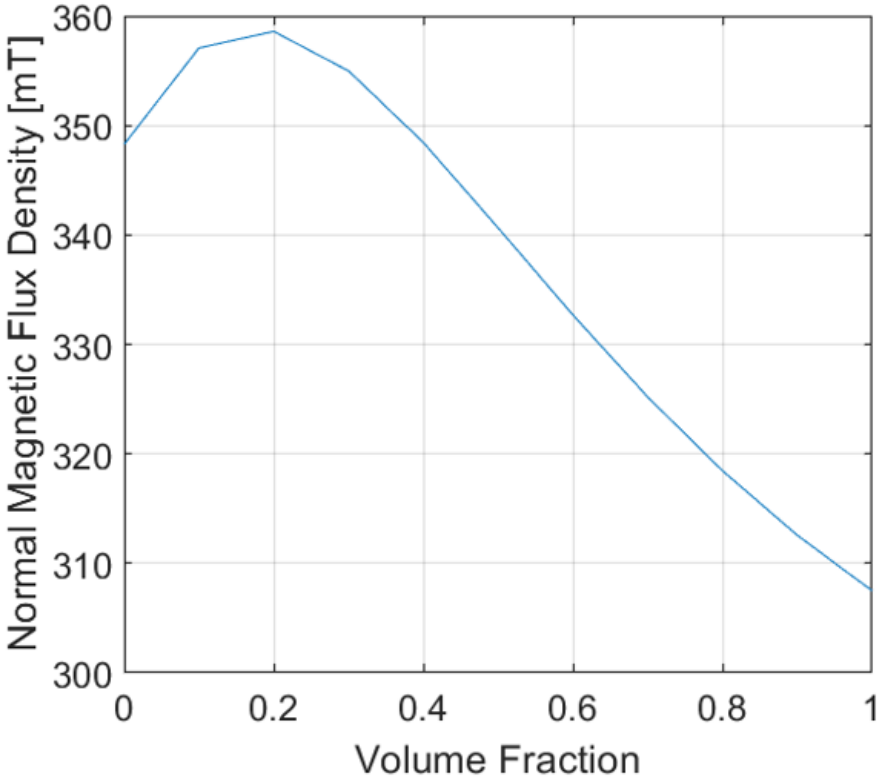

Figure 5.5: The normal magnetic flux density changes based on the volume fraction of embedded MSMA particles in an aluminum-MSMA composite before the austenite to martensite transformation is considered. Increasing the volume fraction of MSMA particles in the composite decreases the normal magnetic flux density as measured externally.

Before considering the change in magnetic flux density due to the phase transformation of embedded MSMA particles in composites, it is important to note that the addition of MSMA particles to an aluminum host will have a tangible effect on the magnetic field regardless of phase. Thus, changes in magnetic flux density can only be attributed to MSMA particle phase transformation if the geometries and composite composition are held constant. For all studies,

these parameters are held constant to allow for the comparison of regions under the same geometries and compositions, providing an untransformed magneto-static solution as a reference. That reference magneto-static field can be seen in Fig. 5.6.

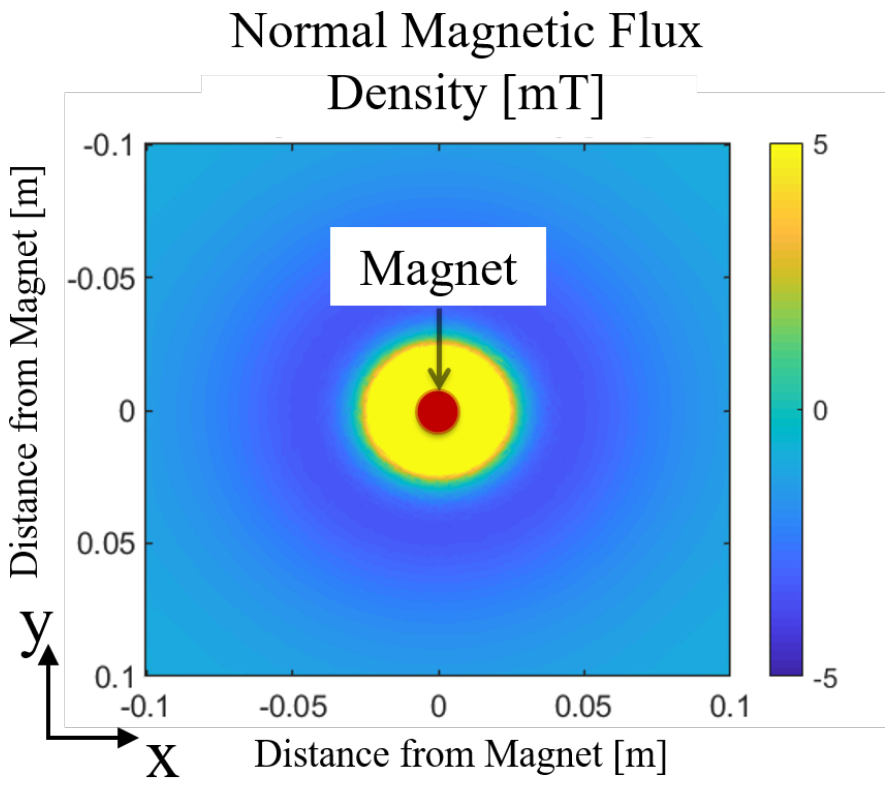

Figure 5.6: The normal magnetic flux density exhibits polar symmetry around the permanent magnet.

5.2.3 The Effects of a Locally Transformed Region of Embedded MSMA Particles in an Aluminum Host

Next, a region of the untransformed composite is replaced with a region of transformed composite. The magnetic flux density of the two magneto-static solutions are compared, and mapped onto the composite surface. The mapped region and transformed region can be seen in Fig. 5.7.

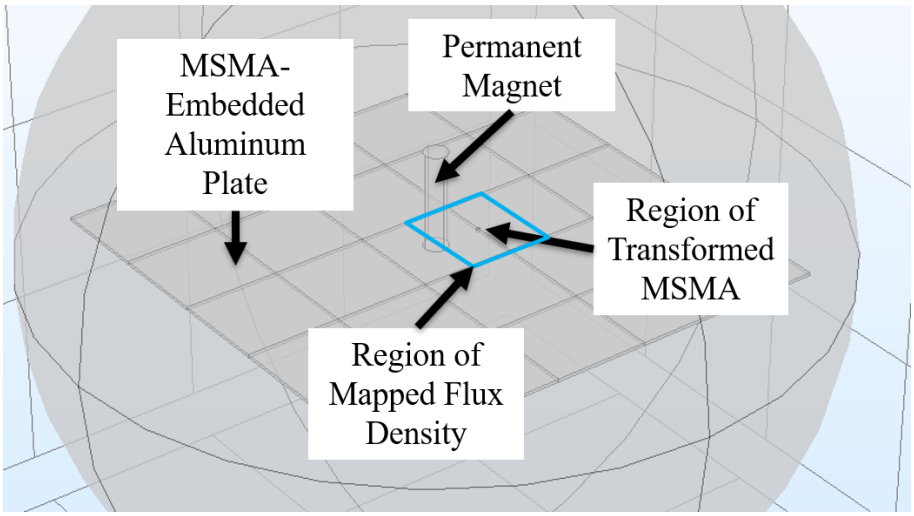

Figure 5.7: A transformed region of the aluminum-MSMA composite is introduced into the magneto-static model, with the magnetic flux density of the nearby region mapped onto the composite surface.

This distribution of magnetic flux density, unlike the previous configurations with a MSMA wire or cable, exhibits polar symmetry due to the homogeneous distribution of particles in the aluminum host.

The mapped change in magnetic flux density occurs around the transformed MSMA region as seen in Fig. 5.8. The normal magnetic flux density fluctuates near the transformed region, increasing inboard of the region while decreasing outboard of the region.

5.3 Overview of Embedded MSMA Particles for Magnetic Sensing

The introduction of MSMA particles into an aluminum sheet will change the magnetic properties of the composite by increasing the magnetic permeability. Under loading near internal cracks or damage, the MSMA particles will transform from austenite to stress-induced martensite near the crack [38]. This change in phase of the individual particles in the MSMA-aluminum composite leads to local changes in the composite magnetic permeability. When the individual particles change magnetic permeability, this leads to a change in an applied magnetic field. This change in magnetic field can be measured on the surface of the composite plate by measuring

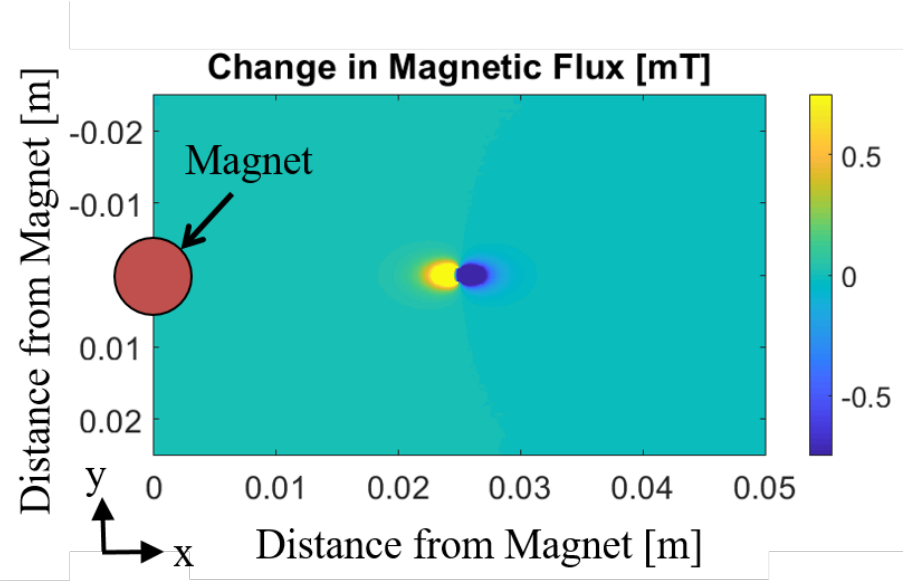

Figure 5.8: The normal magnetic flux density near a region of the composite with transformed MSMA particles fluctuates due to the internal permeability changes of the composite.

the normal magnetic flux density. The magnetic field generated by cylindrical magnet is an axisymmetric field, so changes in a local region that do not match other regions at the same radial distance from the center of the magnet. Local transformation of MSMA particles leads to measurable changes. For a 10% volume fraction of MSMA particles, there is change of over 500 μT near the transformed region of MSMA particles. More work is needed to determine the actual martensite volume fraction ξ generated by a loaded plate with a crack in it based on the geometry, loading, and volume fraction of MSMA particles, but the magneto-static framework is complete to determine the practicality of embedded MSMA particles in an aluminum host for NDE of aircraft.

6. CONCLUSIONS AND FUTURE WORK

6.1 Summary of Research

In this work, a novel technique for non-destructive evaluation of concrete structures via embedded magnetic shape memory alloy (MSMA) reinforcing wires is introduced. Coupled structural and magneto-static modeling tools are developed to determine the effect of internal damage and associated stress concentrations transforming nearby local regions of an embedded MSMA wire from austenite to stress-induced martensite (SIM). The structural analysis framework presented computes the transformation of an initially austenite FeMnAlNi wire embedded in a concrete block under 3-point bending. The block is loaded until the pre-existing crack propagates through the concrete block passing the MSMA wire. This increase in the stress and strain state of the MSMA wire leads to formation of a SIM region near the crack tip, changing the local magnetic properties of the concrete-MSMA composite. A magneto-static model is developed to calculate the change in an externally applied magnetic field due to the internal damage and resulting formation of SIM. The phase transformation is correlated to the change in wire magnetic permeability, and an updated spatial distribution of material magnetic permeability is generated. Studies were then performed to explore the fluctuations in magnetic field caused by the generated local SIM region in the embedded MSMA, and the feasibility of the external magnetic sensing is discussed. It was found that the formation of the SIM region in the embedded MSMA wire can alter the magnetic properties of the concrete-MSMA composite such that in the presence of an externally applied magnetic field, an external location near the SIM region registers a measurable change in normal magnetic flux density. This change can then be correlated to the local phase transformation in the embedded MSMA wire. Combined with the structural reinforcement properties of SMAs laid out in works cited previously, MSMAs may offer an attractive multifunctional embedded sensing component in concrete structures.

In the magnetic sensitivity studies explored, the largest measurable external changes in normal

magnetic flux density due to the SIM region could be measured using the same side sensing configuration, whereby the magnet and sensor are placed near each other on the same surface. As the MSMA components are embedded deeper in a structure, the measurable magnetic sensitivity decreases, eventually limiting the depth of sensing. The same side sensing results also support the exploration of additional sensors arrayed for higher resolution in locating damage. The normal magnetic flux density evaluated at all possible same side sensing locations supports the addition of multiple sensors in an array for higher resolution.

The magneto-static model was then expanded to other form factors, such as embedded particles and braided cables. The effects of SMA phase transformation can be quantified and measured externally. Large grain MSMA wires can be externally analyzed to determine phase transformation by comparing the external magnetic flux density of both an untransformed MSMA wire and the MSMA wire in question. The boundaries between austenite and martensite grains in large grain MSMA wires can also be determined via external magnetic sensing by moving a magnetic/sensor combination down the length of the MSMA wire due to the large fluctuations in local magnetic flux density near such grain boundaries. Embedded MSMA particles can also be used for SHM, and the transformation of MSMA particles from austenite to martensite due to internal cracks will lead to a significant change in measurable magnetic flux density in the region. The computational results in this work support SHM using multi-functional MSMA wires for non-destructive evaluation by characterizing the quantitative change in an externally applied magnetic field due to the transformation of embedded magnetic shape memory alloy components, introducing a method for detecting and evaluating the internal damage in concrete structures via external magnetic sensing.

6.2 Future Work

There are a number of recommendations for future work based off of the results and work presented herein. First, a more thorough exploration of the geometries involved in the transformation of embedded MSMA components would be valuable, as this initial study only looked at a sin-

gle structural boundary value problem outlined in Chapter 3.1. Experimental and computational work to model various other structural loading and damage systems is needed to expand the application to real-world infrastructure. Work on the effect of a crack tip stress field near embedded MSMA particles is currently being conducted, and the results could be input into the magneto-static model for embedded MSMA particles presented in this thesis by mapping the martensite volume fractions from the structural model to the magnetic permeabilities in the magneto-static model.

REFERENCES

[1] N. Malone, P. Miller, H. Ozcan, J. Ma, J. Schaffer, and I. Karaman, "Integrated health monitoring of transportation structures with magnetic fe-sma wires," *MATEC Web of Conferences*, vol. 271, p. 01008, 2019.

[2] J. Fan, D. Jiang, J. Chen, W. Liu, W. Tiedeu Ngaha, and J. Chen, "Fatigue performance of ordinary concrete under discontinuous cyclic loading," *Construction and Building Materials*, vol. 166, pp. 974–981, Mar. 2018.

[3] C. Boller, "Ways and options for aircraft structural health management," *Smart Materials and Structures*, vol. 10, pp. 432–440, June 2001.

[4] B. Rajani and Y. Kleiner, "Non-destructive inspection techniques to determine structural distress indicators in water mains," p. 20, 2004.

[5] B. M. Phares, G. A. Washer, D. D. Rolander, B. A. Graybeal, and M. Moore, "Routine highway bridge inspection condition documentation accuracy and reliability," *Journal of Bridge Engineering*, vol. 9, pp. 403–413, July 2004.

[6] M. Moore, B. M. Phares, B. Graybeal, D. Rolander, and G. Washer, "Reliability of visual inspection for highway bridges, volume i: Final report," June 2001.

[7] F. Tondolo, A. Cesetti, E. Matta, A. Quattrone, and D. Sabia, "Smart reinforcement steel bars with low-cost mems sensors for the structural health monitoring of rc structures," *Construction and Building Materials*, vol. 173, pp. 740–753, June 2018.

[8] E. Verstrynge, K. De Wilder, A. Drougkas, E. Voet, K. Van Balen, and M. Wevers, "Crack monitoring in historical masonry with distributed strain and acoustic emission sensing techniques," *Construction and Building Materials*, vol. 162, pp. 898–907, Feb. 2018.

[9] L. Pahlavan, F. Zhang, G. BlacquiÃĺre, Y. Yang, and D. Hordijk, "Interaction of ultrasonic waves with partially-closed cracks in concrete structures," *Construction and Building Materials*, vol. 167, pp. 899–906, Apr. 2018.

[10] M. Diakhate, N. Angellier, R. Moutou Pitti, and F. Dubois, "On the crack tip propagation monitoring within wood material: Cluster analysis of acoustic emission data compared with numerical modelling," *Construction and Building Materials*, vol. 156, pp. 911–920, Dec. 2017.

[11] S. Masmoudi, A. E. Mahi, S. Turki, and R. E. Guerjouma, "Structural health monitoring by acoustic emission of smart composite laminates embedded with piezoelectric sensor," in *Design and Modeling of Mechanical Systems*, Lecture Notes in Mechanical Engineering, pp. 307–314, Springer, Berlin, Heidelberg, 2013.

[12] J. T. Simonen, M. M. Andringa, K. M. Grizzle, S. L. Wood, and D. P. Neikirk, "Wireless sensors for monitoring corrosion in reinforced concrete members," vol. 5391, pp. 587–597, International Society for Optics and Photonics, July 2004.

[13] G. M. Light, H. Kwun, S.-y. Kim, and R. L. S. Jr, "Method and apparatus for short term inspection or long term structural health monitoring," May 2002.

[14] J. S. Popovics, G. E. Gallo, M. Shelton, and P. L. Chapman, "A magnetic sensing approach to characterize corrosion in reinforced concrete," vol. 6529, p. 65291A, International Society for Optics and Photonics, Apr. 2007.

[15] A. Razmi and M. M. Mirsayar, "On the mixed mode i/ii fracture properties of jute fiber-reinforced concrete," *Construction and Building Materials*, vol. 148, pp. 512–520, Sept. 2017.

[16] X. Shi, M. Mirsayar, A. Mukhopadhyay, and D. Zollinger, "Characterization of two-parameter fracture properties of portland cement concrete containing reclaimed asphalt pavement aggregates by semicircular bending specimens," *Cement and Concrete Composites*, vol. 95, pp. 56–69, Jan. 2019.

[17] J. Duic, S. Kenno, and S. Das, "Performance of concrete beams reinforced with basalt fibre composite rebar," *Construction and Building Materials*, vol. 176, pp. 470–481, July 2018.

[18] A. Nanni, T. Okamoto, M. Tanigaki, and S. Osakada, "Tensile properties of braided frp rods for concrete reinforcement," *Cement and Concrete Composites*, vol. 15, pp. 121–129, Jan. 1993.

[19] E. Choi, B. Mohammadzadeh, D. Kim, and J.-S. Jeon, "A new experimental investigation into the effects of reinforcing mortar beams with superelastic sma fibers on controlling and closing cracks," *Composites Part B: Engineering*, vol. 137, pp. 140–152, Mar. 2018.

[20] R. D. Finlayson, M. Friesel, M. Carlos, P. Cole, and J. C. Lenain, "Health monitoring of aerospace structures with acoustic emission and acousto-ultrasonics," vol. 43, no. 3, p. 4, 2001.

[21] N. Godin, P. Reynaud, and G. Fantozzi, "Challenges and limitations in the identification of acoustic emission signature of damage mechanisms in composites materials," *Applied Sciences*, vol. 8, p. 1267, aug 2018.

[22] V. Giurgiutiu, J. M. Redmond, D. P. Roach, and K. Rackow, "Active sensors for health monitoring of aging aerospace structures," in *Smart Structures and Materials 2000: Smart Structures and Integrated Systems*, vol. 3985, pp. 294–305, International Society for Optics and Photonics, jun 2000.

[23] W. J. Staszewski, S. Mahzan, and R. Traynor, "Health monitoring of aerospace composite structures âĂŞ Active and passive approach," *Composites Science and Technology*, vol. 69, pp. 1678–1685, Sept. 2009.

[24] W. J. Staszewski, B. C. Lee, and R. Traynor, "Fatigue crack detection in metallic structures with lamb waves and 3d laser vibrometry," *Measurement Science and Technology*, vol. 18, pp. 727–739, Jan. 2007.

[25] J. Smithard, N. Rajic, S. van der Velden, P. Norman, C. Rosalie, S. Galea, H. Mei, B. Lin, and V. Giurgiutiu, "An advanced multi-sensor acousto-ultrasonic structural health monitoring system: Development and aerospace demonstration," *Materials*, vol. 10, jul 2017.

[26] C. K. Tan and D. Mba, "Limitation of acoustic emission for identifying seeded defects in gearboxes," *Journal of Nondestructive Evaluation*, vol. 24, pp. 11–28, mar 2005.

[27] E. A. Peraza Hernandez, S. Hu, H. W. Kung, D. Hartl, and E. Akleman, "Towards building smart self-folding structures," vol. 37, pp. 730–742, Oct. 2013.

[28] D. J. Hartl, G. Chatzigeorgiou, and D. C. Lagoudas, "Three-dimensional modeling and numerical analysis of rate-dependent irrecoverable deformation in shape memory alloys," *International Journal of Plasticity*, vol. 26, pp. 1485–1507, Oct. 2010.

[29] J. Pereiro-BarcelÃş and J. L. Bonet, "Ni-ti sma bars behaviour under compression," *Construction and Building Materials*, vol. 155, pp. 348–362, Nov. 2017.

[30] N. K. Simha, P. S. Rama Sreekanth, and S. B. Venkata Siva, "Shape-memory alloys," in *Reference Module in Materials Science and Materials Engineering*, Elsevier, 2017.

[31] J. Sam, B. Franco, J. Ma, I. Karaman, A. Elwany, and J. H. Mabe, "Tensile actuation response of additively manufactured nickel-titanium shape memory alloys," *Scripta Materialia*, vol. 146, pp. 164–168, Mar. 2018.

[32] A. Zafar and B. Andrawes, "Experimental flexural behavior of sma-frp reinforced concrete beam," *Frontiers of Structural and Civil Engineering*, vol. 7, pp. 341–355, Dec. 2013.

[33] L. CortÃl's-Puentes, M. Zaidi, D. Palermo, and E. Dragomirescu, "Cyclic loading testing of repaired sma and steel reinforced concrete shear walls," *Engineering Structures*, vol. 168, pp. 128–141, Aug. 2018.

[34] R. E. McMahon, J. Ma, S. V. Verkhoturov, D. Munoz-Pinto, I. Karaman, F. Rubitschek, H. J. Maier, and M. S. Hahn, "A comparative study of the cytotoxicity and corrosion resistance

of nickelâĂŞtitanium and titaniumâĂŞniobium shape memory alloys," *Acta Biomaterialia*, vol. 8, pp. 2863–2870, July 2012.

[35] B. Zheng and M. Dawood, "Fatigue crack growth analysis of steel elements reinforced with shape memory alloy (sma) fiber reinforced polymer (frp) composite patches," *Composite Structures*, vol. 164, pp. 158–169, Mar. 2017.

[36] J. A. Monroe, I. Karaman, B. Basaran, W. Ito, R. Y. Umetsu, R. Kainuma, K. Koyama, and Y. I. Chumlyakov, "Direct measurement of large reversible magnetic-field-induced strain in niâĂŞcoâĂŞmnâĂŞin metamagnetic shape memory alloys," *Acta Materialia*, vol. 60, pp. 6883–6891, Dec. 2012.

[37] B. Verijenko and V. Verijenko, "A new structural health monitoring system for composite laminates," *Composite Structures*, vol. 71, pp. 315–319, Dec. 2005.

[38] M. M. Mirsayar and D. J. Hartl, "Damage detection via embedded sensory particles âĂŞ effect of particle/matrix interphase properties," *Composite Structures*, vol. 232, p. 111536, jan 2020.

[39] N. M. Bruno, *The magnetocaloric and elastocaloric effects in magnetic shape memory alloys*. Ph.d., Texas A&M University, United States – Texas, 2015.

[40] L. W. Tseng, J. Ma, S. J. Wang, I. Karaman, M. Kaya, Z. P. Luo, and Y. I. Chumlyakov, "Superelastic response of a single crystalline femnalni shape memory alloy under tension and compression," *Acta Materialia*, vol. 89, pp. 374–383, May 2015.

[41] T. Omori, K. Ando, M. Okano, X. Xu, Y. Tanaka, I. Ohnuma, R. Kainuma, and K. Ishida, "Superelastic effect in polycrystalline ferrous alloys," *Science*, vol. 333, pp. 68–71, July 2011.

[42] T. Omori, M. Okano, and R. Kainuma, "Effect of grain size on superelasticity in Fe-Mn-Al-Ni shape memory alloy wire," *APL Materials*, vol. 1, p. 032103, Sept. 2013.

[43] H. Ozcan, J. Ma, S. J. Wang, I. Karaman, Y. Chumlyakov, J. Brown, and R. D. Noebe, "Effects of cyclic heat treatment and aging on superelasticity in oligocrystalline Fe-Mn-Al-Ni shape memory alloy wires," *Scripta Materialia*, vol. 134, pp. 66–70, June 2017.

[44] L. W. Tseng, J. Ma, S. J. Wang, I. Karaman, and Y. I. Chumlyakov, "Effects of crystallographic orientation on the superelastic response of FeMnAlNi single crystals," *Scripta Materialia*, vol. 116, pp. 147–151, Apr. 2016.

[45] K. Haldar, D. C. Lagoudas, and I. Karaman, "Magnetic field-induced martensitic phase transformation in magnetic shape memory alloys: Modeling and experiments," *Journal of the Mechanics and Physics of Solids*, vol. 69, pp. 33–66, Sept. 2014.

[46] I. Karaman, H. E. Karaca, B. Basaran, D. C. Lagoudas, Y. I. Chumlyakov, and H. J. Maier, "Stress-assisted reversible magnetic field-induced phase transformation in ni2mnga magnetic shape memory alloys," *Scripta Materialia*, vol. 55, pp. 403–406, Aug. 2006.

[47] J. R. Rice, R. M. McMeeking, D. M. Parks, and E. P. Sorensen, "Recent finite element studies in plasticity and fracture mechanics," *Computer Methods in Applied Mechanics and Engineering*, vol. 17-18, pp. 411–442, Feb. 1979.

[48] C. Lu, C. K. Y. Leung, and V. C. Li, "Numerical model on the stress field and multiple cracking behavior of engineered cementitious composites (ecc)," *Construction and Building Materials*, vol. 133, pp. 118–127, Feb. 2017.

[49] M. Williams, "On the stress distribution at the base of a stationary crack," *Journal of Applied Mechanics*, vol. 24, no. 79, pp. 109–114, 1957.

[50] M. M. Mirsayar and P. Park, "Mixed mode brittle fracture analysis of high strength cement mortar using strain-based criteria," *Theoretical and Applied Fracture Mechanics*, vol. 86, pp. 233–238, Dec. 2016.

[51] M. M. Mirsayar, A. Razmi, and F. Berto, "Tangential strain-based criteria for mixed-mode i/ii fracture toughness of cement concrete," *Fatigue & Fracture of Engineering Materials &*

Structures, vol. 41, no. 1, pp. 129–137, 2017.

[52] B. R. Bielefeldt, J. D. Hochhalter, and D. J. Hartl, "Shape memory alloy sensory particles for damage detection: Experiments, analysis, and design studies," *Structural Health Monitoring*, vol. 17, pp. 777–814, July 2018.

[53] V. Yamakov, J. Hochhalter, W. Leser, J. Warner, J. Newman, G. Purja Pun, and Y. Mishin, "Multiscale modeling of sensory properties of co-ni-al shape memory particles embedded in an al metal matrix," *Journal of Materials Science*, vol. 51, pp. 1204–1216, Feb. 2016.

[54] W. P. Leser, J. A. Newman, J. D. Hochhalter, V. K. Gupta, and F. G. Yuan, "Embedded niâĂŞti particles for the detection of fatigue crack growth in aa7050," *Fatigue and Fracture of Engineering Materials and Structures*, vol. 39, pp. 686–695, June 2016.

[55] S. Hatefi Ardakani, A. Afshar, and S. Mohammadi, "Numerical study of thermo-mechanical coupling effects on crack tip fields of mixed-mode fracture in pseudoelastic shape memory alloys," *International Journal of Solids and Structures*, vol. 81, pp. 160–178, Mar. 2016.

[56] J. G. Boyd and D. C. Lagoudas, "A thermodynamical constitutive model for shape memory materials. part i. the monolithic shape memory alloy," *International Journal of Plasticity*, vol. 12, pp. 805–842, Jan. 1996.

[57] D. Lagoudas, D. Hartl, Y. Chemisky, L. Machado, and P. Popov, "Constitutive model for the numerical analysis of phase transformation in polycrystalline shape memory alloys," *International Journal of Plasticity*, vol. 32, pp. 155 – 183, 2012.

[58] N. Moes, J. Dolbow, and T. Belytschko, "A finite element method for crack growth without remeshing," p. 20, 1999.

[59] D. Broekaart, "Modelling crack propagation using xfem," March 2017.

[60] S. by Dassault Systemes, "Abaqus unified fea."

[61] T. Belytschko and T. Black, "Elastic crack growth in finite elements with minimal remeshing," *International Journal for Numerical Methods in Engineering*, vol. 45, pp. 601–620, June 1999.

[62] A. S. Shedbale, I. V. Singh, and B. K. Mishra, "Nonlinear simulation of an embedded crack in the presence of holes and inclusions by xfem," *Procedia Engineering*, vol. 64, pp. 642–651, Jan. 2013.

[63] J. Dolbow, N. MoÃńs, and T. Belytschko, "Discontinuous enrichment in finite elements with a partition of unity method," *Finite Elements in Analysis and Design*, vol. 36, pp. 235–260, Nov. 2000.

[64] "Standard test method for flexural strength of concrete (using simple beam with center-point loading)," *American Society for Testing And Materials*, 2018.

[65] R. Narayan Swamy, "Dynamic poisson's ratio of portland cement paste, mortar and concrete," *Cement and Concrete Research*, vol. 1, pp. 559–583, Sept. 1971.

[66] L. W. Tseng, J. Ma, S. J. Wang, I. Karaman, and Y. I. Chumlyakov, "Effects of crystallographic orientation on the superelastic response of femnalni single crystals," *Scripta Materialia*, vol. 116, pp. 147–151, Apr. 2016.

[67] L. W. Tseng, J. Ma, M. Vollmer, P. KrooÃ§, T. Niendorf, and I. Karaman, "Effect of grain size on the superelastic response of a femnalni polycrystalline shape memory alloy," *Scripta Materialia*, vol. 125, pp. 68–72, Dec. 2016.

[68] COMSOL, "Comsol software documentation."

[69] A. N. Lagarkov and A. K. Sarychev, "Electromagnetic properties of composites containing elongated conducting inclusions," *Physical Review B*, vol. 53, pp. 6318–6336, Mar. 1996.

[70] A. N. Lagarkov and K. N. Rozanov, "High-frequency behavior of magnetic composites," *Journal of Magnetism and Magnetic Materials*, vol. 321, pp. 2082–2092, July 2009.

[71] K. Magnetics, "Kj magnetics.com - specifications."

[72] Mathworks, “Matlab documentation,” 2019.

[73] Supermagnete, “Calculate magnetic flux density with formula,” 2018.

[74] R. Popovics, “Hall magnetic sensor devices,” 2017.

[75] LakeShore, “400 series hall probes,” 2019.

[76] M. Magnetics, “Magnetic field microsensor arrays,” 2019.

[77] N. E. Barta and I. Karaman, “Embedded magnetic shape memory sensory particles in lightweight composites for crack detection,” *Materials Science and Engineering: A*, vol. 751, pp. 201–213, Mar. 2019.